IRAQI JOURNAL OF APPLIED PHYSICS

The *Iraqi Journal of Applied Physics (IJAP)* is a peer reviewed journal of high quality devoted to the publication of original research papers from applied physics and their broad range of applications. IJAP publishes quality original research papers, comprehensive review articles, survey articles, book reviews, dissertation abstracts in physics and its applications in the broadest sense. It is intended that the journal may act as an interdisciplinary forum for Physics and its applications. Innovative applications and material that brings together diverse areas of Physics are particularly welcome. Review articles in selected areas are published from time to time. It aims to disseminate knowledge; provide a learned reference in the field; and establish channels of communication between academic and research experts, policy makers and executives in industry, commerce and investment institutions. IJAP is a quarterly specialized periodical dedicated to publishing original papers, letters and reviews in: Applied & Nonlinear Optics, Applied Mechanics & Thermodynamics, Digital & Optical Communications, Electronic Materials & Devices, Laser Physics & Applications, Plasma Physics & Applications, Quantum Physics & Spectroscopy, Semiconductors & Optoelectronics, Solid State Physics & Applications, Alternative & Renewable Energy, and Environmental Science & Technology.

ISSN (Print): 1813-2065, ISSN (Online): 2309-1673, ISSN (Letters): 1999-656X

EDITORIAL BOARD

Raad A. KHAMIS	Asst. Professor	Editor-in-Chief	Plasma Physics	IRAQ
Walid K. HAMOUDI	Professor	Member	Laser Physics	IRAQ
Dayah N. RAOUF	Asst. Professor	Member	Laser and Optics	IRAQ
Raid A. ISMAIL	Professor	Member	Semiconductor Physics	IRAQ
Oday A. HAMMADI	Asst. Professor	Managing Editor	Molecular Physics	IRAQ
Intesar F. RAMLEY	Professor	Member	Communications Eng.	CANADA
Manal J. AL-KINDY	Asst. Professor	Member	Electrical Engineering	IRAQ
Khaled A. AHMED	Professor	Member	Theoretical Physics	IRAQ
Kais A. AL-NAIMEE	Asst. Professor	Member	Quantum Optics	ITALY
Abdulmajeed IBRAHIM	Professor	Member	Solid State Physics	IRAQ
Loay E. GEORGE	Asst. Professor	Member	Computers & Networks	IRAQ
Abdulhadi ALKHALILI	Professor	Member	Medical Physics	U.S.A
Haitham M. MIKHLIF	Lecturer	Member	Molecular Physics	IRAQ

Editorial Office:
P. O. Box 55259, Baghdad 12001, IRAQ
Website: www.iraqiphysicsjournal.com
Emails: info@iraqiphysicsjournal.com, editor_ijap@yahoo.co.uk, ijap.editor@gmail.com,

ADVISORY BOARD

Abdullah M. SUHAIL, Professor, Department of Physics, College of Science, University of Baghdad, IRAQ
Adel K. HAMOUDI, Professor, Department of Physics, College of Science, University of Baghdad, IRAQ
Andrei KASIMOV, Professor, Institute of Material Science, National Academy of Science, Kiev, UKRAINE
Ashok KUMAR, Professor, Harcourt Butler Technological Institute, Kanpur, Uttar Pradesh 208 002, INDIA
Chang Hee NAM, Professor, Korean Advanced Institute of Science and Technology, Daehak-ro, Daejeon, KOREA
Claudia GAULTIERRE, Professor, Faculty of Sciences and Techniques, University of Rouen, Rouen, FRANCE
El-Sayed M. FARAG, Professor, Department of Sciences, College of Engineering, AlMinofiya University, EGYPT
Gang XU, Assistant Professor, Department of Engineering and Physics, University of Central Oklahoma, U.S.A
Heidi ABRAHAMSE, Professor, Faculty of Health Sciences, University of Johannesburg, S. AFRICA
Madis-Lipp KROKALMA, Professor, School of Science, Tallinn University of Technology, 19086 Tallinn, ESTONIA
Mansoor SHEIK-BAHAE, Associate Professor, Department of Physics, University of New Mexico, U.S.A
Mohammad Robi HOSSAN, Assistant Professor, Dept. of Eng. and Physics, Univ. of Central Oklahoma, U.S.A
Mohammed A. HABEEB, Professor, Department of Physics, Faculty of Science, Nahrain University, Baghdad, IRAQ
Morshed KHANDAKER, Associate Professor, Dept. of Engineering and Physics, Univ. of Central Oklahoma, U.S.A
Muhammad A. HUSSAIN, Assistant Professor, Dept. of Laser and Optoelectronics Eng., Nahrain University, IRAQ
Mutaz S. ABDUL-WAHAB, Assistant Professor, Dept. of Electric Engineering, University of Technology, IRAQ
Nadir F. HABOUBI, Professor, Department of Physics, College of Education, Mustansiriya Univ., Baghdad, IRAQ
Qian Wei Chang, Professor, Faculty of Science and Engineering, University of Alberta, Edmonton, Alberta, CANADA
Sebastian ARAUJO, Professor, School of Applied Sciences, National University of Lujan, Buenos Aires, ARGENTINA
Shivaji H. PAWAR, Professor, D.Y. Patil University, Kasaba Bawada, Kolhapur-416 006, Maharashtra, INDIA
Xueming LIU, Professor, Department of Electronic Eng., Tsinghua University, Shuang Qing Lu, Beijing, CHINA
Yanko SAROV, Assistant Professor, Micro- and Nanoelectronic Systems, Technical University Ilmenau, GERMANY
Yushihiro TAGUCHI, Professor, Dept. of Physics, Chuo University, Higashinakano Hachioji-shi, Tokyo, JAPAN

SPONSORED AND PUBLISHED BY
THE IRAQI SOCIETY FOR ALTERNATIVE AND RENEWABLE ENERGY SOURCES & TECHNIQUES (I.S.A.R.E.S.T.)

IRAQI JOURNAL OF APPLIED PHYSICS

ISSN (Print): 1813-2065, ISSN (Online): 2309-1673, ISSN (Letters): 1999-656X

INSTRUCTIONS TO AUTHORS

CONTRIBUTIONS

Contributions to be published in this journal should be original research works, i.e., those not already published or submitted for publication elsewhere, individual papers or letters to editor.
Manuscripts should be submitted to the editor at the mailing address:
Iraqi Journal of Applied Physics, Editorial Board, P. O. Box 55259, Baghdad 12001, IRAQ
Website: www.iraqiphysicsjournal.com
Email: editor@iraqiphysicsjournal.com, editor_ijap@yahoo.co.uk, ijap.editor@gmail.com

MANUSCRIPTS

Two hard copies with soft Word copy on a CD or DVD should be submitted to Editor in the following configuration:

- **One-column** Double-spaced one-side A4 size with 2.5 cm margins of all sides
- Times New Roman font (16pt bold for title, 14pt bold for names, 12pt bold for headings, 12pt regular for text)
- Manuscripts presented in English only are accepted.
- English abstract not exceed 150 words
- 4 keywords (at least) should be maintained on (PACS preferred)
- Author(s) should express all quantities in SI units
- Equations should be written in equation form (*italic* and symbolic) NOT in plain text
- Tables and Figures should be separated from text and placed in new pages after the references
- Charts should be indicated by the software used for generating them (e.g., Excel, MATLAB, Grapher, etc.)
- Figures and diagrams can be submitted in original colored forms for assessment and they will be returned to authors after provide printable copies
- Only original or high-resolution scanner photos are accepted
- For electronic submission, articles should be formatted with MS-Word software.

AUTHOR NAMES AND AFFILIATIONS

It is IJAP policy that all those who have participated significantly in the technical aspects of a paper be recognized as co-authors or cited in the acknowledgments. In the case of a paper with more than one author, correspondence concerning the paper will be sent to the first author unless staff is advised otherwise.
Author name should consist of first name, middle initial, last name. The author affiliation should consist of the following, as applicable, in the order noted:
- Company or college (with department name or company division), Postal address, City, Governorate or State, zip code, Country name, contacting telephone number, and e-mail

REFERENCES

The references should be brought at the end of the article, and numbered in the order of their appearance in the paper. The reference list should be cited in accordance with the following examples:
[1] X. Ning, R. Benford and M.R. Lovell, "On the Sliding Friction Characteristics of Unidirectional Continuous FRP Composites", *J. Tribol. Func. Mater.*, 124(1) (2002) 5-13.
[2] M. Barnes, "Stresses in Solenoids", *J. Appl. Phys.*, 48(5) (2001) 2000–2008.
[3] J. Jones, **"Contact Mechanics"**, Cambridge University Press (Cambridge, UK) (2000), Ch.6, p.56.
[4] Y. Lee, S.A. Korpela and R. Horne, "Structure of Multi-Cellular Natural Convection in a Tall Vertical Annulus", Proceedings of 7th International Heat Transfer Conference, U. Grigul et al., eds., Hemisphere (Washington DC), 2 (1982) 221–226.
[5] M. Hashish, "Waterjet Technology Development", High Pressure Technology, PVP-Vol. 406 (2000) 135-140.
[6] D.W. Watson, "Thermodynamic Analysis", ASME Paper No. 97-GT-288 (1997).
[7] C.Y. Tung, "Evaporative Heat Transfer in the Contact Line of a Mixture", Ph.D. thesis, Rensselaer Polytechnic Institute, Troy, NY (1982).

PROOFS

Authors will receive proofs of papers and are requested to return one corrected copy as a WORD file on a compact disc (CD) or by email. New materials inserted in the original text without Editor's permission may cause rejection of paper.

COPYRIGHT FORM

Author(s) will be asked to sign the IJAP Copyright Form and hence transfer copyrights of the article to the Journal soon after acceptance of it. This will ensure the widest possible dissemination of information.

OFFPRINTS

Authors will receive electronic offprint free of charge and any additional reprints can be ordered.

SUBSCRIPTION AND ORDERS

Annual fees (4 issues per year) of subscription are:
50 US$ for individuals inside Iraq; **200** US$ for institutions inside Iraq;
100 US$ for individuals abroad; **300** US$ for institutions abroad.
Fees are reduced by 25% for I.S.A.R.E.S.T. members. Orders of issues can be submitted by contacting the editor-in-chief or editorial office at admin@iraqiphysicsjournal.com, or editor_ijap@yahoo.co.uk to maintain the address of issue delivery and payment way.

IRAQI JOURNAL OF APPLIED PHYSICS
Vol. 18, No. 4, October-December 2022, pp. 3-8

Saman H. Majeed
Jamal A. Hasan
Eman G. Khalil

[1] *Department of Biomedical Engineering, College of Engineering, Al-Nahrain University, Jadiriya Campus, Baghdad, IRAQ*

Microscopic Imaging of Red Cell Aggregation with Photoacoustic Technique

Photoacoustic Imaging is a hybrid modality of optical contrast and acoustic resolution of a qualitative leap and a new technology for imaging the micro-structure of the blood. The infections and cardiovascular diseases were the main cause of intravascular RBCs aggregations. In this study, the modern detection of RBCs aggregation can be obtained by the combination of photoacoustic technology with artificial intelligence technology. The power of the photoacoustic signal was measured to detect RBCs aggregation that's indicate to ESR value. Analysis of RBCs microscope images by threshold algorithm detects the ratio of red color to other colors or ratio of RBCs to the background (gray level). Thus the evaluation of the RBCs aggregation level is done, which indicates to Erythrocyte Sedimentation Rate (ESR) level. The photoacoustic technique takes about 10 minutes compared to a manual ESR test which takes an hour, also early detects and predicts cardiovascular disorders in future.

Keywords: Artificial Intelligent; Blood Image; Image segmentation; Photoacoustic Microscopic
Received: 21 July 2022; **Revised:** 04 September 2022; **Accepted:** 11 September 2022

1. Introduction

Photoacoustic (PA) imaging is one of the latest technologies in the field of examining and monitoring red blood cells, and knowledge of the functional and morphological (structural) characteristics of those cells by exposing them to the laser Nd:YAG 1064 nm at several minutes [1]. When the ultrasound signals resulting from the absorption of laser energy by the red blood cells, were received at the spectral frequencies through transducer 5Mhz [2]. Also The photoacoustic microscope with artificial intelligence plays a major role in analyzing data and images of RBCs aggregation accurately [3]. The artificial intelligence has begun to exist in several medical fields as a sophisticated technology for deep and rapid analysis, as well as obtaining better results by software algorithms for medical examinations [4]. The threshold algorithm was employed to analyze the PA microscopic images to investigate and predicate the number of clusters, the size level of clusters, clusters density, near the cluster to each other of high or low-density regions, for detection the ESR value (3 -15 mm/hr) [5].

Several studies have been introduced to detect the RBCs aggregation in the blood by using an acousto-optic imaging technique [6], and other introduced procedure entails classifying and segmenting a single RBC image after resizing it to determine the cell's minimum and maximum radius [7], the clusters of red blood cells act as a point to ESR level which was an indicator to detect the type of diseases such as rheumatoid arthritis, inflammations and infection [8].

2. Material and Method

2.1 Prepare the samples and radiation

Blood samples are collected and prepared from 60 subjects and kept in EDTA K3 tubes at room temperature (20° C), then measure the manual ESR value of each blood sample over a one-hour time period [9]. Put the blood sample inside a cubic quartz cuvette (1x1x4 cm^3), then radiate the sample with a laser beam (Nd:YAG 1064nm) with a rate of 6 pulses per second and an energy capacity of 20 mJ at the top area of the cuvette, and receive the photoacoustic signal using transducer 5MHz. For the photoacoustic imaging, uses the optical microscope to assess the ESR value by detecting the RBCs aggregation level of the samples, through performing blood smear on the glass slides, they were examined using a CCD camera attached to the eyepiece microscope, as shown in Fig (1), then the images are processed and analyzed to estimate the RBCs aggregation using threshold algorithms.

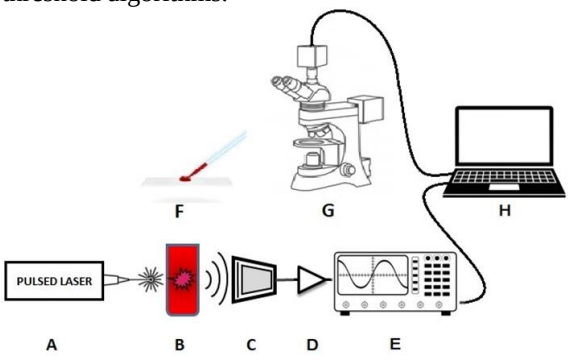

Fig. (1) Schematic photoacoustic system: (A) Nd:YAG laser 1064nm, (B) Cubic quartz cuvette, (C) Transducer, (D) Received circuit (amplifier), (E) Oscilloscope, (F) Glass slide, (G) Optical microscope with CCD camera, (H) laptop.

 © ALL RIGHTS RESERVED

2.2 Photoacoustic signal measurement

The power of photoacoustic signal estimated by ultrasound transducer at 5MHz then amplified the signal via a received circuit, and analyze the power of PA signal to detect the RBCs aggregation. The RBCs aggregation level indicate to the energy absorption ability that generate different ultrasound waves caused the various of power of photoacoustic signals.

2.3 Microscopic images for photoacoustic technique

The images of blood smears provided by a CCD camera (Genex Ltd. - 5mm) attached with the optical microscope (GENEX – OPTIK 20) and the magnification was 40X. The components of photoacoustic microscope system matching with methods of artificial intelligence technology to process the image of RBCs aggregation images, as shown in Fig (2).

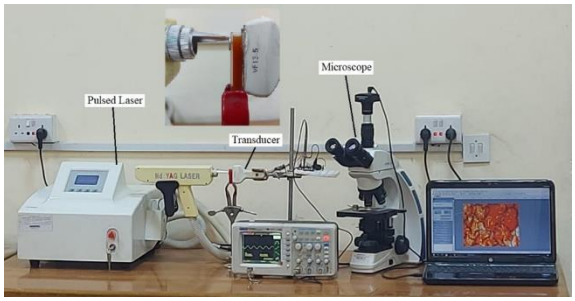

Fig. (2) Photoacoustic components: Nd:YAG laser, cubic cuvette, transducer, received circuit, oscilloscope, optical microscope and laptop

2.3 Image analysis algorithms

The image segmentation algorithm is considered one of the common and modern techniques for microscopy image analysis and digital image processing [10]. Image analysis algorithm based on the pixels of images, after collecting the images through an optical microscope and storing, then the sequence algorithms are used in bioinformatics for cluster analysis of RBCs aggregation. The image segmentation concludes separate the region of interest (ROI) from the background, several algorithms involved the auto-threshold segmentation technique [11].

Threshold Algorithms:

Thresholding is one of the simple algorithms for image segmentation, it is characterized by its speed. This method assumes that the images consist of different areas of gray levels and color levels. The histogram consists of peaks values that represent the color densities of the images [12]. The pixels of colors of the boundary object are divided into two densities. The first act as an object (ROI) which is higher or equal to or less than the second-pixel density, which represents the background. This is proved by selecting the appropriate threshold value, to determine those differences after converting the pixels to black and white when converting the image to binary, or by selecting one color which was sensitive to the algorithm [13]. Several methods exist for image segmentation, depending on the difference between white and black color as a basis for the work, or relying on the density of the gray color [14].

The current study shows the detection of the apparent and clustering areas of RBCs by algorithms depending on the color difference in the image by two groups of segmentation techniques as shown in Fig (3). It proposing a method which segment and identify varied RBCs in blood smear images which is agree with S. Rahman [15].

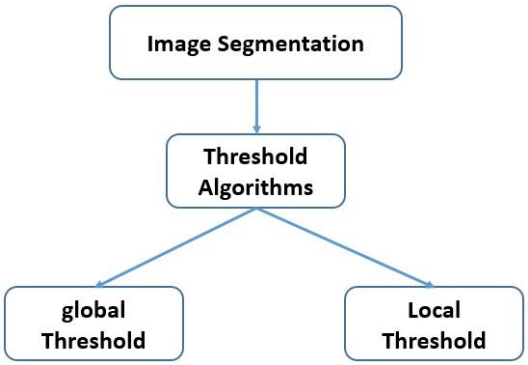

Fig. (3) Threshold algorithm techniques

The Common Threshold Algorithms are:

1- A global threshold technique: This algorithm depends on using only one threshold value to segment each image [16].

2- Local threshold technique (multi-threshold): This is based on the conversion of the color image into binary image mode. In the local threshold technique, the unique threshold values for the partitioned sub-images are obtained from the whole image. Commonly, the whole image pixels are scanned to classify the pixels into object or the background, based on the gray-level value compared to the threshold function [17]. The steps of the threshold algorithms are explained in the flowcharts as shown in Fig (4).

The object and background pixels in the global are represented as two groups of gray levels acting as the two main modes, white pixels (WP) and black pixels (BP). While the obvious method in the multi-threshold distinguish the object (R1) from the background by selecting a threshold T then Tnew, that separates color modes of image intensity between 0 to 255 color brightness as shown in Fig (5).

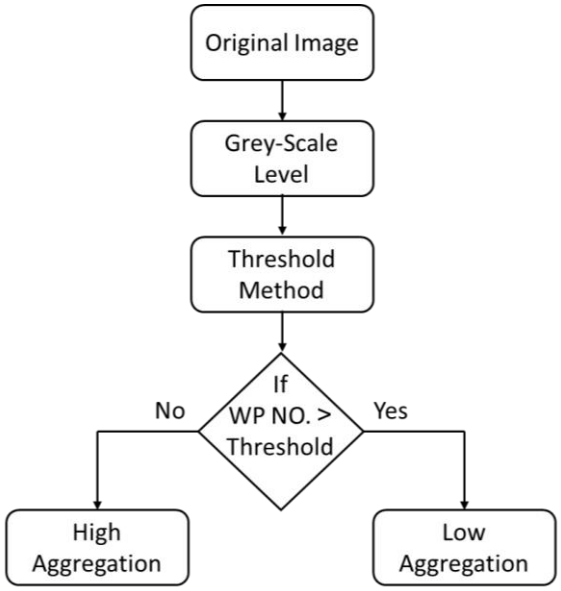

(a)

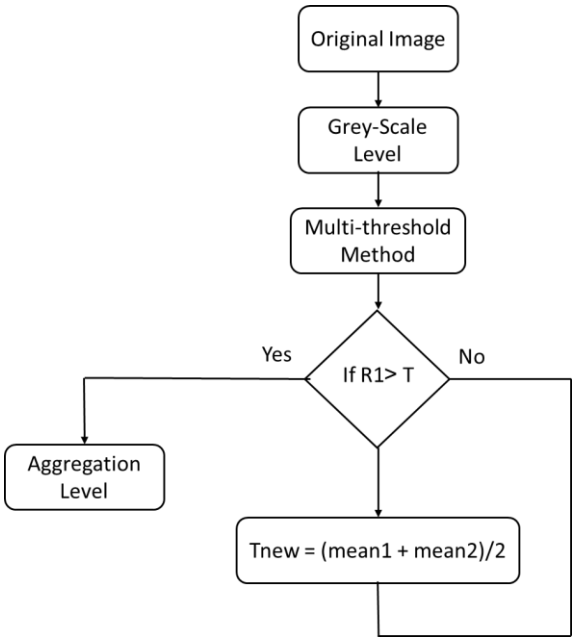

(b)

Fig. (4) Flowcharts of (a) global threshold segmentation algorithm, and (b) local (multi) threshold technique

The image which contains multi-regions can be segmented by using multi-threshold algorithm, in multi-regions, it is possible to model the images by multi-threshold algorithm [18]. The histogram modes become more difficult to identify as the number of regions increase, and threshold selection becomes more complicated [16].

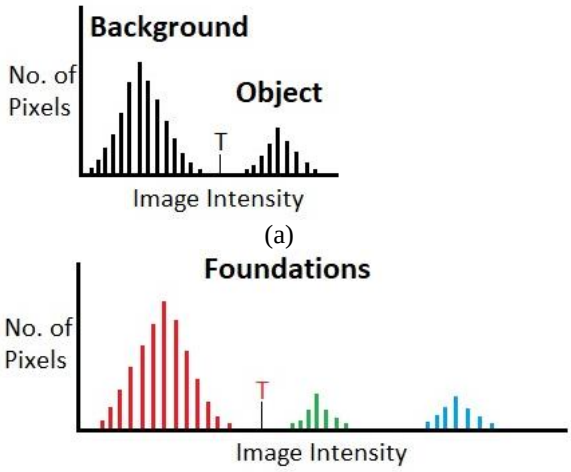

(a)

(b)

Fig. (5) The histogram of threshold algorithms: (a) global threshold, and (b) local threshold

3. Results and Discussion

The mean power of photoacoustic amplitude signals were obtained from (60) blood samples then measured the standard deviation (SD) to each sample, the results demonstrated that the power spectrum related to the size of the observer gradually increased as the level of aggregation increased; the mean power spectrum values at a hematocrit of 40% for RBCs suspensions (1.1 to 22 dB) at low RBCs aggregation and high RBCs aggregation respectively. The validity of the photoacoustic accuracy to detect the aggregation level manifested through the comparison of PA signal analysis with the manual ESR test results are shown in Fig (6).

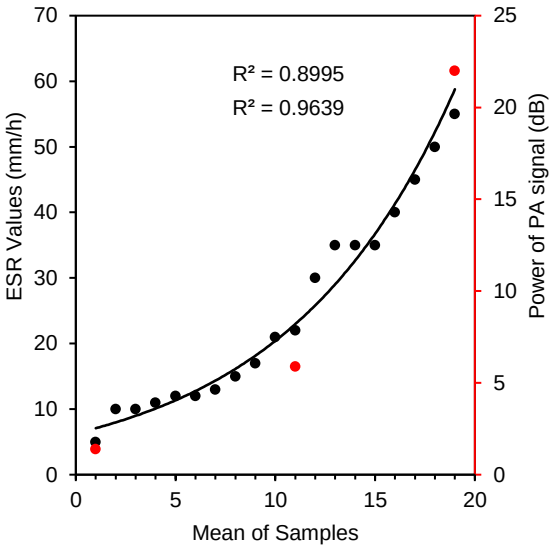

Fig. (6) Chart comparison the power of PA signal and manual ESR values

The analysis of the photoacoustic microscopic images by global threshold is a computationally simple and fast method because it was a single threshold T value that compares between the background and the object as shown in Fig (7).

 © ALL RIGHTS RESERVED

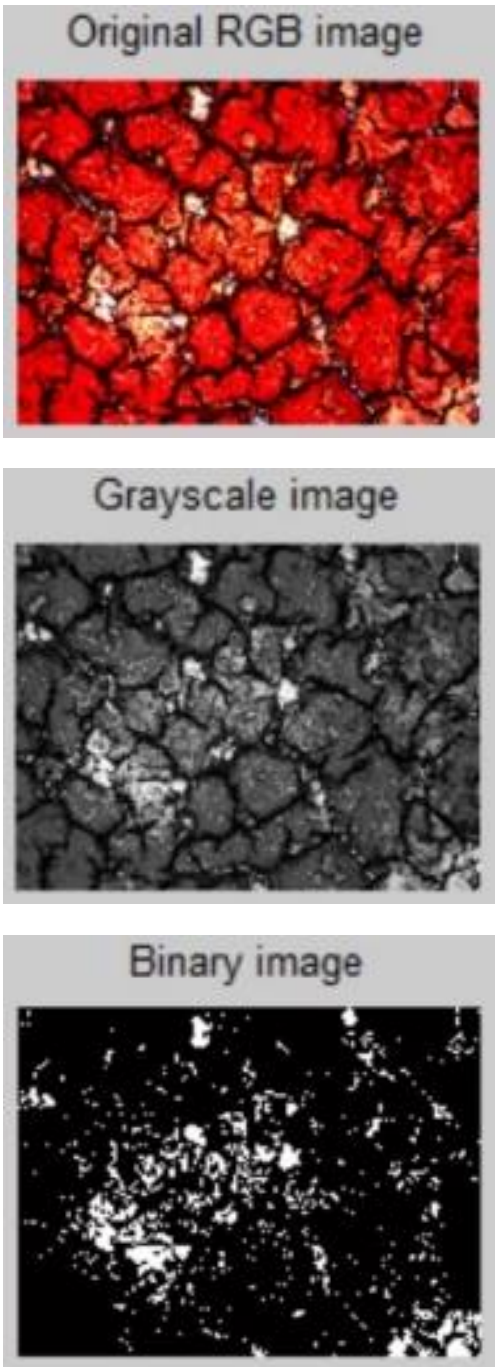

Fig. (7) Detect RBCs aggregation by using a global threshold algorithm

The histogram of the global threshold distinguishes the object (as a dark color) from the background (as a light color) in the image as shown in Fig (8)

The local multi-threshold algorithm was more flexible for detecting the red color pixels when the different red levels were found by the multi-threshold value levels Red- Green- Blue (RGB) colors for each image range from 0 to 255 color brightness as shown in Fig (9).

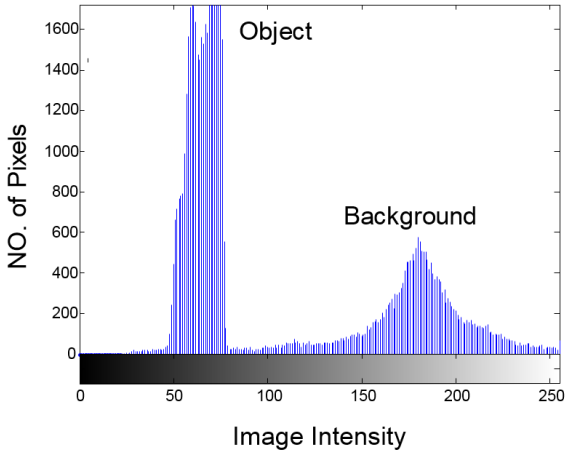

Fig. (8) Histogram of global threshold algorithm

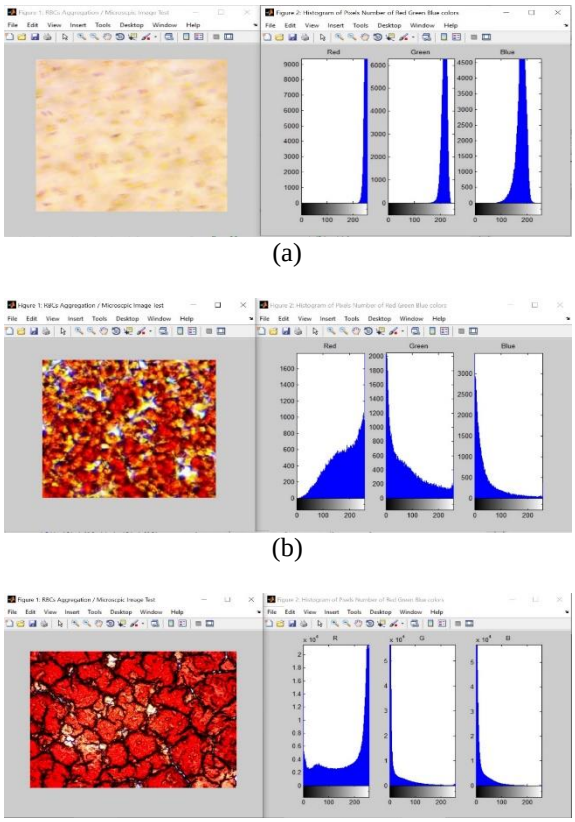

(a)

(b)

(c)

Fig. (9) Detection the colors level of microscopic image by using multi threshold algorithm and histogram (a) Low red color density in the image (483x466 pixels), (b) Increase red color density in the image (362x317 pixels), (c) High red color density scale in the image (1280x916 pixels)

The mean and the ratio of red pixels were higher than those of the other colors pixels within the (RGB) image, that indicates to the high RBCs aggregation and it means an increase in ESR value, while a decrease in the red pixels means reducing the ESR value, as shown in Fig (10).

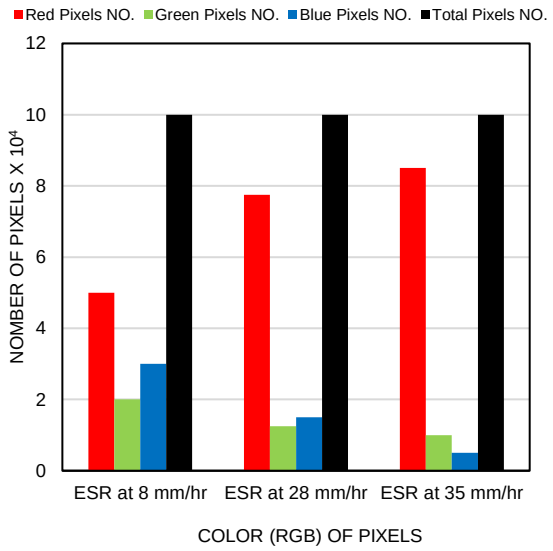

Fig. (10) Relation between ESR value and color pixels number of image

The validity of photoacoustic imaging results to detect the RBCs aggregation level with respect to the manual ESR test can be described in a comparison shown in Fig (11)

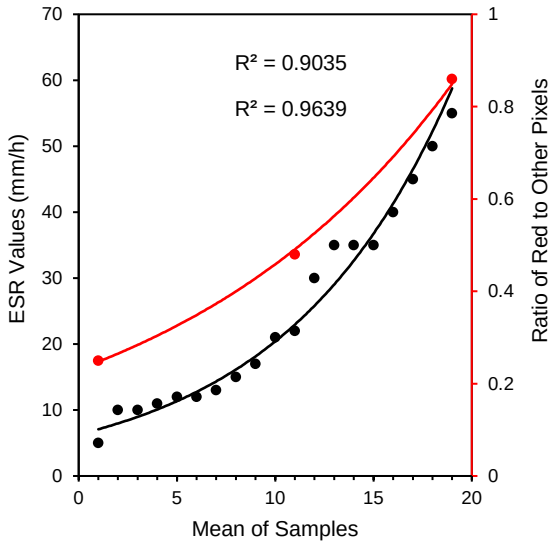

Fig. (11) Chart comparison (ratio red to other pixels) and manual ESR values

As shown in the results of photoacoustic signal and imaging figures (6) and (11), respectively, the accuracy of detecting the ESR value is acceptable when compared with manual ESR test as shown in table (1).

4. Conclusion

The analysis of photoacoustic (PA) signal and RBCs images by the photoacoustic technique is consider to enhance the functional and structural of photoacoustic system, which evaluate the power of PA signal and analysis the RBCs images into the color pixels and gray level pixels and detect the ratio of red color to other colors and evaluate the level RBCs aggregation, which points to Erythrocyte Sedimentation Rate (ESR) level. Finally, the photoacoustic technique is able to detect the erythrocytes aggregation quickly and accurately, this is an important advantage in the medical laboratory tests.

Table (1) The level of RBCs aggregation in the manual ESR test, the power of photoacoustic signals analysis and photoacoustic imaging analysis, with the time they take.

Test	Manual ESR method	Power of the photoacoustic signal analysis	Photoacoustic imaging analysis
RBCs aggregation	96%	90%	90%
Time	1 hour or 2 hours	10 minutes	10 minutes

References

[1] A.B.E. Attia, G. Balasundaram and M. Moothanchery, "A review of clinical photoacoustic imaging: Current and future trends", *Photoacoustics*, 16 (2019) 100-144, doi: 10.1016/j.pacs.2019.100144.

[2] E.M. Strohm, M.J. Moore and M.C. Kolios, "Single Cell Photoacoustic Microscopy: A Review", 22(3) (2016) 6801215.

[3] N. Dey, A.S. Ashour and V.E. Balas, Eds, **"Soft Computing Based Medical Image Analysis"**, Academic Press, (2018) 3-11.

[4] K. Hajdowska, S. Student and D. Borys, "Graph based method for cell segmentation and detection in live-cell fluorescence microscope imaging", *Biomed. Signal Process. Control*, 71A (2022) 103071, doi: 10.1016/j.bspc.2021.103071.

[5] X. Chen, "An efficient multilevel thresholding image segmentation method based on the slime mould algorithm with bee foraging mechanism: A real case with lupus nephritis images", *Comput. Biol. Med.*, 142 (2022) 105179, doi: https://doi.org/10.1016/j.compbiomed.2021.105179.

[6] F. Mohammed, J.A. Hasan and E. Ghadhban, "Development of the determination of ABO and Rh systems of blood group typing using acousto-optical technique Development RI the Determination of ABO and Rh Systems of Blood Group Typing Using Acousto-Optical Technique", *AIP Cofn. Proc.*, 2372 (2021) 030002.

[7] S.M. Mazalan, N.H. Mahmood and M.A.A. Razak, "Automated red blood cells counting in peripheral blood smear image using circular hough transform", *1st Int. Conf. on Artif. Intel. Model. Simul.*, 2013, 320-324, doi:

 © ALL RIGHTS RESERVED

10.1109/AIMS.2013.59.

[8] S.S. Long, L.K. Pickering and C.G. Prober, **"Principles and Practice of Pediatric Infectious Disease",** 3rd ed., Churchill Livingstone (Edinburgh, 2008) 1368-1381.

[9] S.S. Long, **"288 - Laboratory Manifestations of Infectious Diseases"**, 4th ed., S. Long (ed.), Elsevier (London, 2012) 1400-1412.

[10] L. Tan and J. Jiang, **"Digital Signal Processing"**, 2nd ed., Academic Press (Boston, 2013) 683-765, doi.org/10.1016/B978-0-12-415893-1.00014-7.

[11] P. Bhattacharya, K. Edwards and K. Schmid, "Segmentation methods and morphometry of confocal microscopy imaged corneal epithelial cells", *Contact Lens Anterior Eye*, (2022), doi: 10.1016/j.clae.2022.101720.

[12] O. Oleksiuk et al., "Single-molecule localization microscopy allows for the analysis of cancer metastasis-specific mirna distribution on the nanoscale", *Oncotarget*, 6(42) (2015) 44745-44757, doi: 10.18632/oncotarget.6297.

[13] A. Norouzi et al., "Medical image segmentation methods, algorithms, and applications", *IETE Tech. Rev.*, 31(3) (2014) 199-213, doi: 10.1080/02564602.2014.906861.

[14] P. Gyawali et al., "Quantitative Measurement of Erythrocyte Aggregation as a Systemic Inflammatory Marker by Ultrasound Imaging: A Systematic Review," *Ultrasound in Med. Biol.*, 44(7) (2018) 1303-1317, doi: 10.1016/j.ultrasmedbio.2018.02.020.

[15] S. Rahman et al., "Automatic identification of abnormal blood smear images using color and morphology variation of RBCS and central pallor", *Comput. Med. Imaging Graph.*, 87 (2021) 101813, doi: 10.1016/j.compmedimag.2020.101813.

[16] J. Rogowska, **"Handbook of Medical Image Processing and Analysis"**, 2nd ed., I.N. Bankman (ed.), Academic Press (Burlington, 2009) 73-90.

[17] N. Dey et al., **"Soft Computing Based Medical Image Analysis"**, Academic Press (NY, 2018) 163-181.

[18] E.R. Davies, **"Computer and Machine Vision"**, 4th ed., Academic Press (Boston, 2012) 82-110.

IRAQI JOURNAL OF APPLIED PHYSICS
Vol. 18, No. 4, October-December 2022, pp. 9-14

Highly-Pure Nanostructured Metal Oxide Multilayer Structure Prepared by DC Reactive Magnetron Sputtering Technique

Asraa M. Hameed
Mohammed A. Hameed

Department of Physics, College of Science, University of Baghdad, Baghdad, IRAQ

In this work, metal oxides nanostructures, mainly, copper oxide (CuO), nickel oxide (NiO), titanium dioxide (TiO_2), and multilayer structure were synthesized by dc reactive magnetron sputtering technique. The structural purity and nanoparticle size of the prepared nanostructures were determined. The individual metal oxide samples (CuO, NiO and TiO_2) showed high structural purity and minimum particle sizes of 34, 44, 61 nm, respectively. As well, the multilayer structure showed high structural purity as no elements or compounds other than the three oxides were founds in the final sample while the minimum particle size was 18 nm. This reduction in nanoparticle size can be considered as an advantage for the dc reactive magnetron sputtering technique when metal oxide multilayer structures are prepared.

Keywords: Nanostructures; Metal oxides; Reactive sputtering; Structural characterization
Received: 01 September 2022; **Revised:** 08 October 2022; **Accepted:** 15 October 2022

1. Introduction

Metal oxides are a rich family of materials that have served many research areas, from colossal magnetoresistance to multiferroicity and from catalysts to wearable devices [1]. Mostly, metal oxides have many advantages like switching time, color variation, good stability, reliability, etc. These oxides are capable of redox reactions that result in color change [2]. The properties of such materials make the transition metal oxides highly desired in energy applications [3]. Oxide materials in bulk and thin film forms, as well as metal oxide nanostructures, exhibit a great variety of functional properties [4].

Nanostructured metal oxides with unique optical, electrical and molecular properties along with desired functionalities and surface charge properties provide interesting platforms [5]. By the control of size, structure, composition and morphology, nanostructured metal oxides can possess novel optical, electronic, magnetic, and/or mechanical properties that are not provided by bulk forms [1,4].

Synthesis and preparation of metal oxide nanostructures are the first and main step to control their properties. Therefore, over more than three decades, methods and techniques for synthesis and preparation of these nanostructures have been designed, employed and optimized [6-8]. Two main classifications are currently known; physical vapor deposition (PVD) and chemical vapor deposition (CVD). Among PVD methods and techniques, dc reactive sputtering has provided many advantages over the others. Sputtering was first observed in 1852 using a dc gas discharge tube by Grove [9,10]. In general, PVD is atomistic deposition process in which the material is vaporized from particle source in the form of atoms or molecules, transported in the form of a vapor through a low pressure gaseous (or plasma) environment to the substrate where it condenses [11]. As the prepared film thickness is required to be highly controlled, magnetron sputtering technique makes a good solution in addition to the high deposition rates and low substrate heating. Also, the optimization of magnetron sputtering parameters, such as substrate temperature, sputtering power, inter-electrode distance, total gas pressure and reactive gas pressure, can be considered to obtain thin films with excellent physical properties [12,13]. This sputtering process basically involves the creation of plasma by applying voltage between the target and the substrate, the target being used as the cathode and the substrate being used as the anode [14]. The molecules are formed before reaching the substrate surface [15].

The sputtered target can be an elemental, alloy, mixture, or compound and the material is vaporized retaining the composition of the bulky target [16]. In reactive sputtering, compound thin films are deposited in the presence of a reactive gas. The reactive gas reacts with the sputtered material and forms a compound. This process makes it possible to deposit a wide variety of compounds (oxides, nitrides, carbides, etc.) with a wide range of properties [17,18]. Figure (1) illustrates the reactive sputtering process. In a magnetron sputtering, the high electric field arising from the cathode fall potential accelerates secondary electrons in a direction normal to the target surface [19].

 © ALL RIGHTS RESERVED

The principal advantage of the magnetron sputtering configuration is that a dense plasma can be formed near the cathode at low pressures [20]. Also, due to the advantages of magnetron sputtering such as preparation of high quality defect-free films, high deposition rate, easy control of elemental composition and structure of the growing film, it is widely used in various industrial applications [21].

2. Experimental Part

A homemade dc reactive magnetron sputtering system schematically shown in Fig. (1) was used in this work to prepare metal oxide thin films and multilayer structure on glass substrates. Highly-pure (99.99%) sheets of copper (Cu), nickel (Ni) and titanium (Ti) were used as sputtering targets in presence of oxygen to deposit CuO, NiO and TiO_2 thin films as well as multilayer structure from these three compounds on glass substrates.

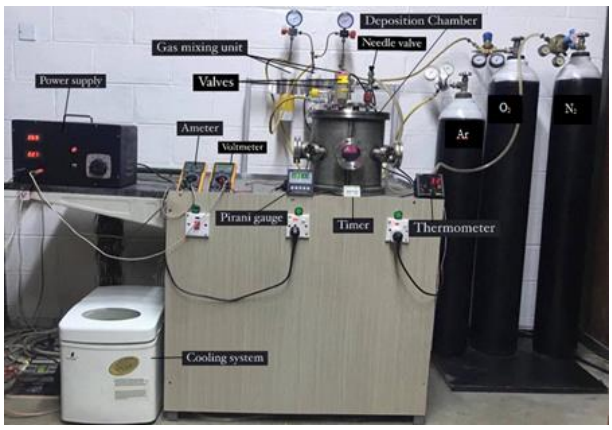

Fig. (1) A photograph of the dc reactive magnetron sputtering system used in this work

The targets were cleaned and dried for the deposition process. The glass substrates used for deposition of the thin films and multilayer structure were initially cleaned before the experiments. The target was maintained carefully on the cathode. The plasma required for sputtering was generated by the electric discharge of argon. Electrical power was provided by a high-voltage dc power supply (up to 5kV). The operation conditions of the system were divided into two groups; constant and variable. The constant operation conditions include vacuum pressure, current-limiting resistance, discharge voltage, discharge current, deposition temperature, inter-electrode distance and gas flow rate, and gas mixing ratio. The variable operation conditions were reduced to the deposition time of 1, 1:30, 2, 2:30 and 3 hours. The multilayer structure was deposited at different deposition times, first layer was CuO for 1 hour, second layer was NiO for 1:30 hours and the last layer was TiO_2 for 2 hours.

Many experiments were performed to determine the optimum working pressure as well as the optimum mixing ratio of Ar and O_2 gases. Also, the optimum inter-electrode distance was determined between 1 to 10 cm and from the experiments results, 4 cm has been specified as the optimum inter-electrode distance. The optimum discharge current was determined according to the stability of the discharge plasma. The deposition chamber was initially evacuated down to 0.001 mbar and then filled with gas mixture of argon and oxygen with mixing ratio of 50:50. The pressure of gas mixture was about 0.15 mbar and the discharge current was 40 mA. The discharge voltage was maintained at 3.5 kV. The two electrodes could be cooled by circulating water from chiller into cooling channels inside both electrodes. The cathode was cooled to prevent the secondary electron emission, which consumes an amount of discharge power, while the anode was not cooled to support the adhesion of metal oxide film to the glass substrate. More details on this sputtering system can be found elsewhere [22-25].

The nanopowders were extracted from thin film samples and multilayer structure by a novel technique known as conjunctional freezing-assisted ultrasonic extraction to extract nanopowders from thin films deposited by PVD methods on non-metallic substrates [26,27].

The structural characteristics of the prepared thin films were determined by x-ray diffraction (XRD), field-emission scanning electron microscopy (FE-SEM), and energy dispersive x-ray spectroscopy (EDS).

3. Results and Discussion

Figure (2) shows the XRD patterns of CuO, NiO, TiO_2 thin films and multilayer structure prepared in this work in order to study the structural properties. It is clear that all samples exhibit high structural purity as no peaks belonging to other materials than CuO, NiO and TiO_2 were observed.

In the XRD pattern of CuO sample, the peak observed at 38.7° and 61.5° were indexed as (111) and (220) crystal planes, which are attributed to the formation of Cu_2O, while the peaks observed at 32.5°, 35,5°, 46.2°, 48.7°, 53.4°, 58.3°, 66.2°, 72.3° and 75°, those corresponding to (-110), (002), (-112), (-202), (202), (-311), (311) and (400) crystal planes, are matched with the values of monoclinic CuO phase [28]. Therefore, the transformation from CuO to Cu_2O phase was confirmed. This transformation can be attributed to the thermal effect caused by increasing the temperature of anode on which the glass substrate is placed. This temperature was measured to reach 80 °C during the deposition process using a thermocouple on the anode surface. Cooling the anode did not prevent the formation of Cu_2O phase, however, its peak intensities were lowered.

The XRD pattern of NiO sample is shown in Fig. (2b). Five distinct diffraction peaks can be seen at 37.35°, 43.38°, 62.9°, 75.46° and 79.42°, those correspond to (111), (200), (220), (311) and (222)

crystal planes. This result has confirmed the formation of polycrystalline NiO compound according to the JCPDS Card No. 73-1519 [23].

The XRD pattern of TiO_2 sample showed that the sample contains of both anatase and rutile phases (mixed-phase) (Fig. 2c). The diffraction peaks at 25.2°, 38.19°, 48.2°, 54.0°, 62.8°, 68.8° and 70.4°, corresponding to (101), (004), (200), (105), (118), (116) and (220) crystal planes, are assigned for the anatase (A) phase. Similarly, the diffraction peaks at 27.6°, 36.2°, 41.4°, 44.2, 54.4°, 56.7 and 64.1, corresponding to crystal planes of (110), (101), (111), (210), (211), (220) and (310), are assigned to the rutile (R) phase according to the JCPDS Card No. 88-1175 [29]. The formation of rutile phase is a consequence of thermally induced transformation of the metastable anatase phase into stable rutile phase. Such transformation is unavoidable within the range of anode's temperature range. However, this transformation can be reasonably reduced by cooling and using of appropriate heat sink during deposition process [30-33].

The XRD pattern of the multilayer structure prepared from CuO/NiO/TiO_2 thin films deposited on glass substrate. All peaks observed in this pattern are belonging to CuO, Cu_2O, NiO and TiO_2 compounds only, as shown in Fig. (2d). No peaks belonging to other materials were observed. In this pattern, seven diffraction peaks of CuO, seven diffraction peaks of TiO_2, four diffraction peaks of NiO, and only one diffraction peak of Cu_2O were observed. This result initially highlights the structural purity of the prepared multilayer structure as the thin films were sequentially deposited. This can be an important advantage of the dc reactive sputtering system used in this work.

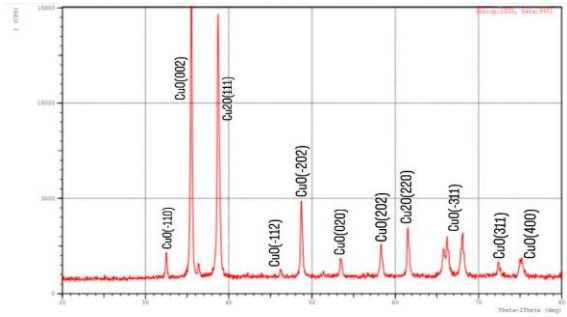

(a) CuO thin film sample

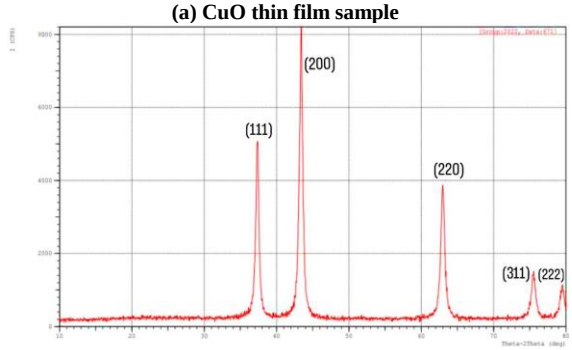

(b) NiO thin film sample

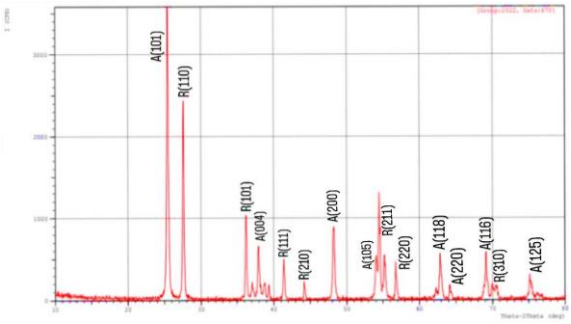

(c) TiO_2 thin film sample

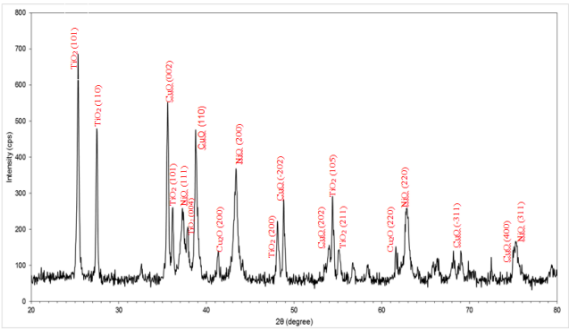

(d) Multilayer structure

Fig. (2) XRD patterns of thin film samples prepared in this work (a) CuO thin film (b) NiO thin film, (c) TiO_2 thin films (d) multilayer structure

The surface profile and particle size of the prepared thin film samples were determined by field-effect scanning electron microscopy (FE-SEM) as shown in Fig. (3). The CuO sample showed an agglomerated surface with minimum particle size of about 34 nm, as shown in Fig. (3a). The deposition process causes the Cu atoms to have enough activation energy, so that the CuO thin films have a higher densification, a larger particle size, and a greater roughness. The NiO sample showed much uniform profile than CuO sample with minimum particle size of 44 nm, as shown in Fig. (3b). As well, the TiO_2 sample showed similar profile as NiO sample with minimum particle size of 61 nm, as shown in Fig. (3c). The observation of some large nanoparticles may be attributed to the fact that nanoparticles have the tendency to agglomerated due to their high surface energy and high surface tension of the ultrafine nanoparticles.

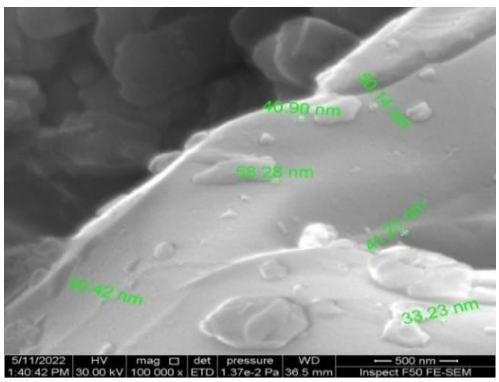

(a) CuO thin film sample

 © ALL RIGHTS RESERVED

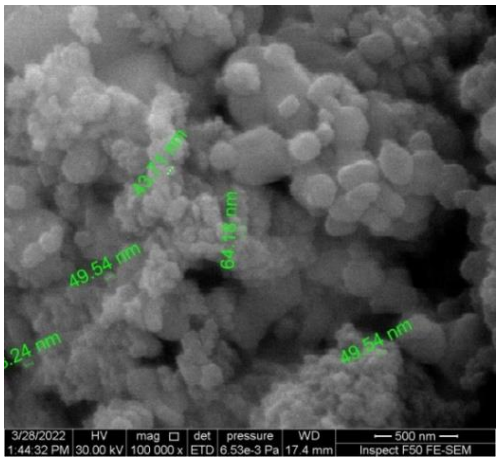

(b) NiO thin film sample

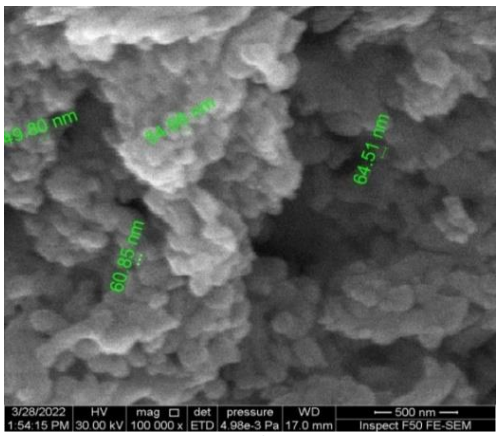

(c) TiO_2 thin film sample

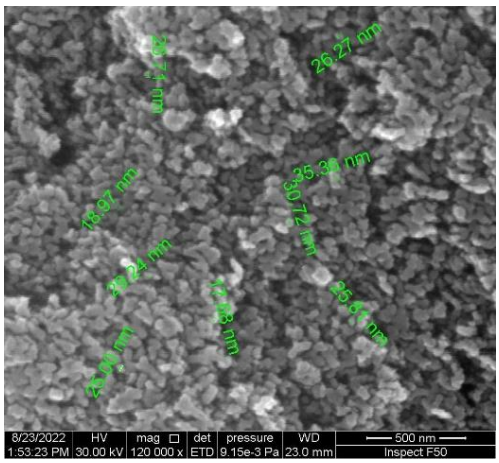

(d) Multilayer structure

Fig. (3) The FE-SEM images of the (a) CuO sample, (b) NiO sample, (c) TiO_2 sample and (d) multilayer structure prepared in this work using 50:50 gas mixture

The FE-SEM image of the ternary multilayer sample shown in Fig. (3d) confirmed the reasonable homogeneous profile with minimum particle size of 18 nm. It is clear that the particle size was decreased when compared to the single thin films because of controlling the operation parameters and preparation conditions, especially the deposition time. Therefore, some advantages can be provided by the multilayer structure to dominate some disadvantages of single compound films. Some practical applications have invested such multilayer structures and their advantages, such as optical filters, heterojunction devices and tracing and marking devices [34,35].

In order to confirm the high structural purity of the prepared samples, the EDX spectra were recorded for CuO, NiO, TiO_2 and multilayer samples, as shown in Fig. (4). Each single thin film sample showed high structural purity as no other elements than the metal and oxygen were detected. Furthermore, the three metallic elements (Cu, Ni and Ti) and oxygen were the only constituents of the multilayer sample. The differences in peak intensities can be attributed to the electronegativity of metallic elements and their tendencies to chemical bonding with oxygen during deposition process. Again, this may confirm the advantages of dc reactive sputtering system used in this work to prepare nanostructured thin films of high quality for many applications those are based on the high structural purity of the functional materials [36,37].

The FE-SEM/EDX mapping for ternary structure revealed that the main elements in the final product are cooper, nickel, titanium and oxygen, as shown in Fig. (5a). The green points refer to O, as shown in Fig. (5b), the red points refer to Cu, as shown in Fig. (5c), the pink points refer to Ni, as shown in Fig. (5d), and the violet points refer to Ti, as shown in Fig. (5e).

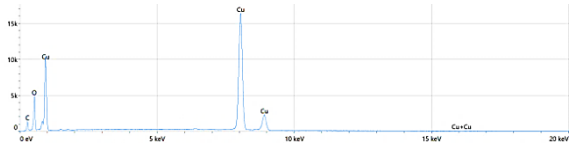

(a) CuO sample

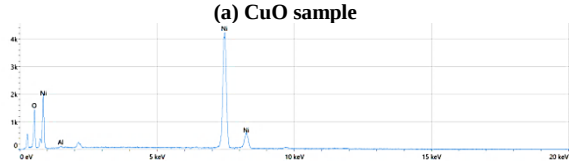

(b) NiO sample

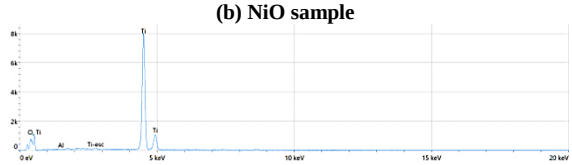

(c) TiO_2 sample

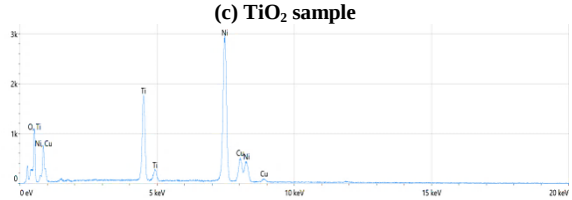

(d) Multilayer structure

Element	Atomic %	Weight %
O	51.1	22.8
Ti	11.4	15.2
Ni	32.0	52.3
Cu	5.5	9.7

(e) Table of weight ratio

Fig. (4) Results of EDX of the (a) CuO sample, (b) NiO sample, (c) TiO_2 sample and (d) structure prepared in this work using 50:50 gas mixture, and (e) table of atomic and weight ratios

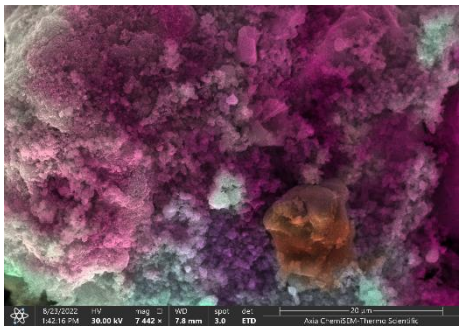

(a) Multilayer structure

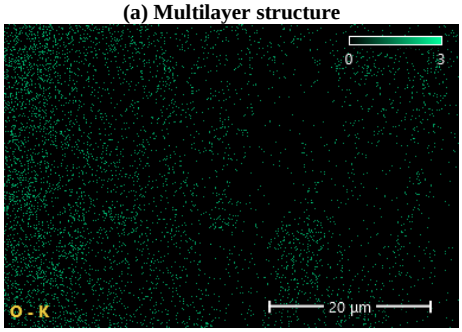

(b) Oxygen

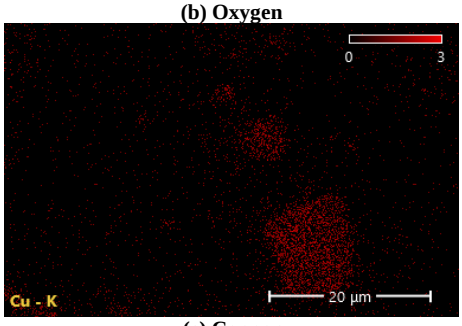

(c) Copper

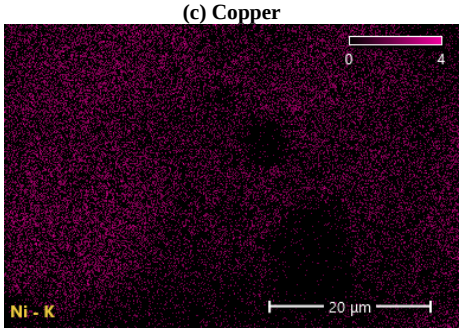

(d) Nickel

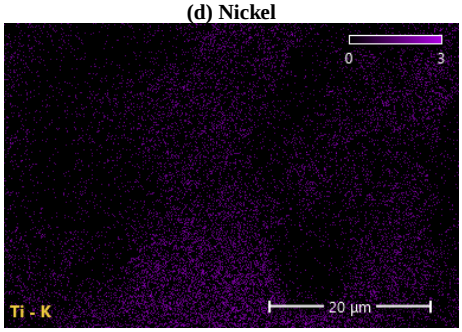

(e) Titanium

Fig. (5) FE-SEM/EDX mapping results of (a) multilayer structure, (b) green pattern refers to O, (c) red pattern refers to Cu, (d) pink pattern refers to Ni, and (e) violet pattern refers to Ti

According to the color distribution ratio in the multilayer sample, the availability of oxygen (O) is the highest (51.1 atomic %) and this is obvious as the oxygen exists in all three compounds forming the multilayer structure. The availability of nickel (Ni) is 32.0 atomic %, the availability of titanium (Ti) is 11.4 atomic %, and finally, the availability of copper (Cu) is the lowest (5.5 atomic %). These differences may be attributed to the density of each layer in the final sample as the film thicknesses were not the same. However, the elemental constitution of a multilayer structure can be reasonably controlled to satisfy the requirements of certain applications.

4. Conclusion

In concluding remarks, metal oxide nanostructures with high structural purity were prepared by dc reactive magnetron sputtering technique. As well, a multilayer structures were prepared from these metal oxide nanostructures. These multilayer structures were highly-pure as no other elements than copper, nickel, titanium and oxygen were found in the final sample. Also, no compounds other than copper oxide, nickel oxide and titanium dioxide were found in the final sample. Such multilayer structures can be successfully employed in many practical applications those based on the structural purity of the functional materials.

References

[1] Z. Yan et al., "Multifunctionalization of nanostructured metal oxides", *J. Nanomater.*, 2015 (2015).

[2] C.G. Granqvist, **"Handbook of Inorganic Electrochromic Materials"**, 1st ed. (1995).

[3] P.M.S. von Monk, R.J. Movtirner and D.R. Rosseinsky, **"Electrochromism: Fundamentals and Applications"**, (1996).

[4] M.L. Grilli, "Metal oxides", *Metals* 10.6 (2020) 820.

[5] P.R. Solanki et al., "Nanostructured metal oxide-based biosensors", *NPG Asia Materials*, 3.1 (2011) 17-24.

[6] M.A. Hameed and Z.M. Jabbar, "Preparation and Characterization of Silicon Dioxide Nanostructures by DC Reactive Closed-Field Unbalanced Magnetron Sputtering", *Iraqi J. Appl. Phys.*, 12(4) (2016) 13-18.

[7] M.A. Hameed and Z.M. Jabbar, "Optimization of Preparation Conditions to Control Structural Characteristics of Silicon Dioxide Nanostructures Prepared by Magnetron Plasma Sputtering", *Silicon*, 10(4) (2018) 1411-1418.

[8] B.K. Nasser and M.A. Hameed, "Structural Characteristics of Silicon Nitride Nanostructures Synthesized by DC Reactive Magnetron Sputtering", *Iraqi J. Appl. Phys.*, 15(4) (2019) 33-36.

[9] K. Wasa, **"Handbook of Sputter Deposition Technology"**, 2nd ed. (2012).

[10] L.J. Gauckler and D. Perednis, "Thin Film Deposition Using Spray Pyrolysis," *J. Electroceram.*, 14(2) (2004) 103-111.

 © ALL RIGHTS RESERVED

[11] P.M. Martin, **"Introduction to Surface Engineering and Functionally Engineered Materials"**, Ch. 6, John Wiley & Sons, Inc., (NJ, 2011) 339.
[12] A.S. Reddy, H.-H. Park and V.S. Reddy, "Effect of sputtering power on the physical properties of dc magnetron sputtered copper oxide thin films", *Mater. Chem. Phys.*, 110(2-3) (2008) 397-401.
[13] F.K. Mugwang'a et al., "Optical characterization of Copper Oxide thin films prepared by reactive dc magnetron sputtering for solar cell applications", *Int. J. Thin Film Sci. Tech.*, 2(1) (2013) 15-24.
[14] W.R. Grove, "VII. On the electro-chemical polarity of gases", *Philo. Trans.*, 142 (1997) 87-101.
[15] D. Güttler, "An Investigation of Target Poisoning during Reactive Magnetron Sputtering", Ph.D. thesis, Universität Dresden (Germany, 2009).
[16] S. Ricciardi, "Surface Chemical Functionalization based on Plasma Techniques", Ph.D. thesis, Politecnico di Torino (Italy, 2012).
[17] P. Carvalho et al., "Influence of the chemical and electronic structure on the electrical behavior of zirconium oxynitride films", *J. Appl. Phys.*, 103(10) (2008) 104907.
[18] L. Combadiere and J. Machet, "Reactive magnetron sputtering deposition of TiN films. I. Influence of the substrate temperature on structure, composition and morphology of the films", *Surf. Coat. Technol.*, 88 (1997) 17-27.
[19] K. Seshan, **"Handbook of Thin Film Deposition: Techniques, Processes, and Technologies**", Ch. 4, 3rd ed., William Andrew, (Amsterdam, 2012) .
[20] D. Mattox, **"Handbook of Physical Vapor Deposition (PVD) Processing",** Ch. 7, 2nd ed., William Andrew, (Amsterdam, 2010).
[21] S. Zenkin, "Reactive magnetron sputtering of thin films with unique properties", Ph.D. thesis, Západočeská univerzita v Plzni (Czech, 2017).
[22] O.A. Hammadi et al., "Magnetic Field Distribution of Closed-Field Unbalanced Dual Magnetrons Employed in Plasma Sputtering Systems", *Iraqi J. Appl. Phys.*, 12(3) (2016) 35-42.
[23] O.A. Hammadi et al., "Employment of Magnetron to Enhance Langmuir Probe Characteristics of Argon Glow Discharge Plasma in Sputtering System", *Iraqi J. Appl. Phys.*, 12(4) (2016) 19-28.
[24] E.A. Al-Oubidy and F.J. Al-Maliki, "Effect of Gas Mixing Ratio on Energy Band Gap of Mixed-Phase Titanium Dioxide Nanostructures Prepared by Reactive Magnetron Sputtering Technique", *Iraqi J. Appl. Phys.*, 14(4) (2018) 19-23.
[25] F.J. Al-Maliki and E.A. Al-Oubidy, "Effect of gas mixing ratio on structural characteristics of titanium dioxide nanostructures synthesized by DC reactive magnetron sputtering", *Physica B: Cond. Matter*, 555 (2019) 18-20
[26] O.A. Hammadi, "Production of Nanopowders from Physical Vapor Deposited Films on Nonmetallic Substrates by Conjunctional FreezingAssisted Ultrasonic Extraction Method", *Proc. IMechE, Part N, J. Nanomater. Nanoeng. Nanosys.*, 232(4), 135-140 (2018).
[27] O.A. Hammadi, "Effects of Extraction Parameters on Particle Size of Titanium Dioxide Nanopowders Prepared by Physical Vapor Deposition Technique", *Plasmonics*, 15 (2020).
[28] Y. Abboud et al., "Biosynthesis, characterization and antimicrobial activity of copper oxide nanoparticles (CONPs) produced using brown alga extract (Bifurcaria bifurcata)", *Appl. Nanosci.*, 4(5) (2014) 571-576.
[29] K. Thamaphat, P. Limsuwan and B. Ngotawornchai, "Phase Characterization of TiO_2 Powder by XRD and TEM", *Kasetsart J. (Nat. Sci.)*, 42 (2008) 357-361.
[30] V. Patil et al., "Effect of Annealing on Structural, Morphological, Electrical and Optical Studies of Nickel Oxide Thin Films", *J. Surf. Eng. Mater. Adv. Technol.*, 1 (2011) 35-41.
[31] O.A. Hammadi, F.J. Kadhim and E.A. Al-Oubidy, "Photocatalytic Activity of Nitrogen-Doped Titanium Dioxide Nanostructures Synthesized by DC Reactive Magnetron Sputtering Technique", *Nonl. Opt. Quantum Opt.*, 51(1-2) (2019) 67-78.
[32] F.J. Al-Maliki, O.A. Hammadi and E.A. Al-Oubidy, "Optimization of Rutile/Anatase Ratio in Titanium Dioxide Nanostructures prepared by DC Magnetron Sputtering Technique", *Iraqi J. Sci.*, 60(special issue) (2019) 91-98.
[33] E.A. Al-Oubidy and F.J. Al-Maliki, "Photocatalytic activity of anatase titanium dioxide nanostructures prepared by reactive magnetron sputtering technique", *Opt. Quantum Electron.*, 51(1-2) (2019) 23.
[34] F.J. Al-Maliki et al., "Enhanced photocatalytic activity of Ag-doped TiO_2 nanoparticles synthesized by DC Reactive Magnetron Co-Sputtering Technique", *Opt. Quantum Electron.*, 52 (2020) 188.
[35] S.H. Faisal and M.A. Hameed, "Heterojunction Solar Cell Based on Highly-Pure Nanopowders Prepared by DC Reactive Magnetron Sputtering", *Iraqi J. Appl. Phys.*, 16(3) (2020) 27-32.
[36] R.H. Turki and M.A. Hameed, "Spectral and Electrical Characteristics of Nanostructured NiO/TiO_2 Heterojunction Fabricated by DC Reactive Magnetron Sputtering", *Iraqi J. Appl. Phys.*, 16(3) (2020) 39-42.
[37] M.A. Hameed, S.H. Faisal, R.H. Turki, "Characterization of Multilayer Highly-Pure Metal Oxide Structures Prepared by DC Reactive Magnetron Sputtering Technique", *Iraqi J. Appl. Phys.*, 16(4) (2020) 25-30

IRAQI JOURNAL OF APPLIED PHYSICS
Vol. 18, No. 4, October-December 2022, pp. 15-19

Ferrohydrodynamic Instability of a Couple Stress Magnetic Fluid Layer Under the Influence of Time-Dependent Sinusoidal Magnetic Field

Balaji Chandrashekar
Rudresha Chandrappa
Vidya Shree Venkatesh
Maruthamanikandan Sokalingam

Department of Mathematics, School of Engineering, Presidency University, Bengaluru, Karnataka 560 064, INDIA

The commencement of convective motion in a horizontal couple-stress ferrofluid exposed to magnetic field modulation has been examined. Making use of isothermal boundary condition, the subsequent eigenvalue problem is attacked by adopting regular perturbation technique with minimum modulation amplitude. Thermal Rayleigh number correction is determined by the modulation frequency, magnetic force, couple-stress parameter and Prandtl number. The impact of various physical factors is perceived to be significant at intermediate magnetic field modulation frequency. It is found that by fine tuning the modulated magnetic frequency, we could either speed up or slow down the commencement of ferroconvection. The problem sheds some light on ferromagnetic fluid applications with a time-varying magnetic field.

Keywords: Ferromagnetic fluid; Magnetic field modulation; Perturbation technique; Stability
Received: 03 September 2022; **Revised:** 8 October 2022; **Accepted:** 15 October 2022

1. Introduction

Ferromagnetic liquids are a type of smart liquid magnetized by magnetic fields and are made by dissolving microscopic magnetic (iron-Fe, cobalt-Co, nickel-Ni, etc.) granules in a non-magnetic liquid transporter (ester, petrol, hydrocarbons, etc.) and wrapping these granules in a surfactant-like organic solution to prevent granule aggregation in the presence of a magnetic field. Many researchers and technologists, however, are fascinated by colloidal magnetite (Fe_3O_4), the most thoroughly studied ferrofluid, due to its diverse applications in thermal engineering, bio-medical, and aerospace [1-3]. The notion of ferroconvection to thermal expansion in a layer enclosing ferrofluid is comparable to the conventional Bènard convection and has sparked considerable interest in the literature due to its potential value as a heat exchanger.

Finlayson first described how an advection of magnetic liquid with variability in magnetic susceptibility yields a non-uniformity in magnetic body force, resulting in thermomagnetic convection [4]. Many researchers, drawing sufficient inspiration from the work of Finlayson, have examined the ferroconvective instability problem under a variety of handy constraints [5-10]. More recently, it has been revealed by means of the higher order Galerkin technique that the influence of MFD viscosity on ferroconvection in a porous medium subjected to varying gravity field delays the onset of ferroconvection [11].

Modulation of an appropriate parameter may have significant effects on the motion of various sectors, such as charges in an electrode material and ferromagnetic resonant, and can result in greater system's stability. The alteration in the magnetic field with respect to time on the threshold of ferroconvection and the conflict between harmonic and sub-harmonic modes using the Floquet theory has been examined in some detail [12-14]. Depending on the frequency of the external magnetic field, the advent of thermo-magnetic convection of magnetic fluid significantly affected by stationary and periodically modulated magnetic field shows a shift in the onset of convection [15,16]. The rate of temperature distribution through an electrically charged couple stress liquid under the influence of magnetic field fluctuation with internal heat source is discussed in detail [17]. Of late, the ferroconvection problem of a sparsely packed porous layer subjected to time-dependent magnetic field has been investigated by means of the regular perturbation method with the assumption of minimum amplitude of modulation [18].

On the other hand, if we combine additives or suspensions in oil/fluid, the fluid forces resist the effect of additives. This resistance produces a couple force, which induces couple stresses throughout the fluid. Owing to the microrotation of colloidal particles, these liquids distort and develop a spin field. The spin field projected by the microrotation of the freely floating polar molecules creates an anti-symmetric tension termed as couple stress, and such fluids are recognized as couple stress fluids. It serves applicability in a variety of industrial processes, including crystalline solidification, polymeric fluid

 © ALL RIGHTS RESERVED

extrusion, exotic lubricants, freezing of metallic plates in a bath, and microscopic solutions, to name a few.

The flow act of non-Newtonian couple stress fluids cannot be effectively characterized by conventional continuum hypothesis. The micro-continuum hypothesis due to Stokes allows for the formation of body couplings, couple stresses, and non-symmetric tensors [19,20]. Assuming a longitudinal wavelength and a negligible Reynolds number, it is reported that the couple stress model produces a larger pressure rise under a given set of conditions when compared to Newtonian fluid models [21]. A mathematical computation concerning squeeze films in a finite bearing system lubricated via couple stress liquids by incorporating the Stokes micro-continuum principle has been investigated in detail [22]. Convective instability of couple stress fluid subjected to rotation, porous medium, chemical reaction and g-jitter has been examined in some detail by a number of researchers [23-27]. Recently, a theoretical study dealing with the effect of rotational modulation on heat and mass transfer in a Darcy porous medium with a couple stress fluid using Ginzburg-Landau approach have been carried out [28].

The problem of convection control is relevant and interesting in a wide range of ferromagnetic fluid applications, not to mention the complexity associated with its mathematical modelling. It should be mentioned that the unmodulated Rayleigh-Bénard problem of ferromagnetic fluid convection subjected to one or more handy constraints has been dealt with by numerous researchers. The effect of magnetic field modulation on Rayleigh-Bénard convection in a horizontal layer of couple stress ferromagnetic fluids, on the other hand, has only received a bit of attention. Motivated by these gaps, we investigate the problem of Rayleigh-Bénard convection in a ferromagnetic couple stress fluid layer induced by magnetic field modulation in this paper, with a focus on how the stability criterion for the onset of ferroconvection changes in the presence of both the couple stress effect and magnetic field modulation.

2. Mathematical Formulation of the Problem

Figure (1) shows the schematic view of the ferroconvection problem's geometric layout. Under the existence of a fluctuated magnetic field, we assess an electrically non-conducting, incompressible, ferromagnetic couple stress liquid trapped between two horizontal surfaces at z=0 and z=d.

A Cartesian setup (x, y, z) is adopted, with the origin at the bottom of the fluid layer and the z-axis working vertically upstream, in the opposite direction of gravity $\vec{g} = -g\hat{k}$. At a constant temperature gradient ΔT, both surfaces are kept warm. The mathematical governing equations of the present study under the Boussinesq approximation are [4,19]

$$\nabla \cdot \vec{q} = 0 \quad (1)$$

$$\rho_0 \left[\frac{\partial \vec{q}}{\partial t} + (\vec{q}\cdot\nabla)\vec{q}\right] = -\nabla p + \rho\vec{g} + \mu_f \nabla^2\vec{q} + \nabla\cdot(\vec{H}\vec{B}) - \mu_C \nabla^4\vec{q} \quad (2)$$

$$C_1\left[\frac{\partial T}{\partial t} + (\vec{q}\cdot\nabla)\vec{H}\right] + \mu_0 T\left(\frac{\partial \vec{M}}{\partial T}\right)_{V,H}\cdot\left[\frac{\partial \vec{H}}{\partial t} + (\vec{q}\cdot\nabla)\vec{H}\right] = K_1\nabla^2 T \quad (3)$$

$$\rho = \rho_0[1-\alpha(T-T_a)] \quad (4)$$

$$\vec{M} = \frac{\vec{H}}{H}M(H,T) \quad (5)$$

$$M = M_0 + \chi_m(H-H_0) - K_m(T-T_a) \quad (6)$$

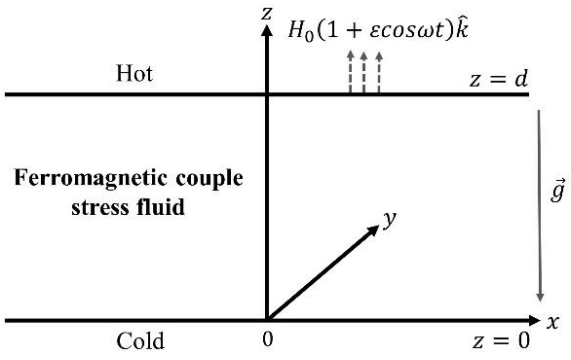

Fig. (1) Geometric configuration of the problem

The relevant Maxwell equations are

$$\nabla\cdot\vec{B} = 0, \nabla\times\vec{H} = 0, \vec{B} = \mu_0(\vec{H}+\vec{M}) \quad (7)$$

where $\vec{q}$ is the velocity of fluid, ρ the density, ρ_0 a reference density, p the pressure, μ_f the fluid viscosity, μ_C the couple stress viscosity, μ_0 the magnetic permeability, T the temperature, $\vec{H}$ the total magnetic field, $\vec{M}$ the magnetization, $\vec{B}$ the magnetic induction, α the coefficient of thermal expansion, T_a a reference temperature, $C_1 = \rho_0 C_{V,H} - \mu_0\vec{H}\cdot\left(\frac{\partial\vec{M}}{\partial T}\right)_{V,H}$, $C_{V,H}$ the specific heat at constant volume and magnetic field, χ_m is the differential magnetic susceptibility and K_m is the pyromagnetic coefficient. The lower and upper surface temperatures respectively are $T = T_a + \frac{1}{2}\Delta T$ at z=0 and $T = T_a - \frac{1}{2}\Delta T$ at z=d.

The external magnetic force is modulated harmonically in time by varying the magnetic field acting vertically upward

$$\vec{H}_0^{ext}(t) = H_0^{ext}(t) = H_0(1+\varepsilon\cos\omega t)\hat{k} \quad (8)$$

where H_0 is the uniform magnetic field, ε is the small amplitude, ω is the frequency and t is the time

3. Linear Stability Theory

On applying the method of small perturbation and introducing the magnetic potential ϕ, we obtain the following stability equations [4,18,31]

$$\left(\frac{1}{\mathrm{Pr}}\frac{\partial}{\partial t} - \nabla^2 + C\nabla^4\right)\nabla^2 W = [R + RM_1(1+\varepsilon F)^2]\nabla_1^2 T - RM_1(1+\varepsilon F)^2\frac{\partial}{\partial z}(\nabla_1^2\phi) \quad (8)$$

$$\left(\frac{\partial T}{\partial t} - W\right) = \nabla^2 T \quad (9)$$

$$\nabla^2\phi = \frac{\partial T}{\partial z} \quad (10)$$

where $F=Re\{e^{-i\omega t}\}=\cos\omega t$, ω is the dimensionless modulation frequency, $\nabla_1^2=\frac{\partial^2}{\partial x^2}+\frac{\partial^2}{\partial y^2}$ and $\nabla^2=\nabla_1^2+\frac{\partial^2}{\partial z^2}$. The dimensionless parameters appearing in Eqs. (8) through (10) are as follows: *Pr* the Prandtl number, *R* the thermal Rayleigh number, *k* the effective thermal diffusivity, M_1 the magnetic number, RM_1 the magnetic Rayleigh number, *C* the couple stress parameter

Equations (8-10) are to be solved using suitable boundary conditions [29]

$$W=\frac{\partial^2 W}{\partial z^2}=T=\frac{\partial\phi}{\partial z}=0 \ at \ z=0,1 \qquad (11)$$

It is suitable to rewrite the entire problem in terms of the vertical component of the velocity *W*. Upon combining Eqs. (8-10), we obtain the following equation

$$\left(\frac{1}{\Pr}\frac{\partial}{\partial t}-\nabla^2+C\nabla^4\right)\left(\frac{\partial}{\partial t}-\nabla^2\right)\nabla^4 W=R\nabla^2\nabla_1^2 W+RM_1(1+\varepsilon F)^2\nabla_1^4 W \qquad (12)$$

The boundary conditions in Eq. (11) can also be rearranged in terms of *W* in the form [30]

$$W=\frac{\partial^2 W}{\partial z^2}=\frac{\partial^4 W}{\partial z^4}=\frac{\partial^6 W}{\partial z^6}=\frac{\partial^8 W}{\partial z^8}=0 \ at \ z=0,1 \qquad (13)$$

4. Method of Solution

The eigenfunctions, *W* and the eigenvalues, *R* associated with the above eigenvalue problem for a modulated magnetic field that is different from the constant magnetic field by means of small quantity of order ε. Therefore, we assume the solution of Eq. (12) of the form [31]

$$\left.\begin{aligned} W&=W_0+\varepsilon W_1+\varepsilon^2 W_2+\cdots\\ R&=R_0+\varepsilon R_1+\varepsilon^2 R_2+\cdots \end{aligned}\right\} \qquad (14)$$

where R_0 is the critical Rayleigh number pertaining to the unmodulated problem. The expression for R_0 is given by

$$R_0=\frac{(\pi^2+\alpha^2)^4+C(\pi^2+\alpha^2)^5}{\alpha^2[\pi^2+(1+M_1)\alpha^2]} \qquad (15)$$

Following the analysis of [31,32], we obtain the following expression for R_2

$$R_2=-\frac{2R_0^2M_1^2\alpha^6}{[\pi^2+(1+M_1)\alpha^2]}\sum_{n=1}^{\infty}\frac{G_n}{J_n} \qquad (16)$$

where

$$G_n=\left(-\frac{1}{\Pr}\omega^2(n^2\pi^2+\alpha^2)^2+(n^2\pi^2+\alpha^2)^4+C(n^2\pi^2+\alpha^2)^5-R_0\alpha^2[n^2\pi^2+(1+M_1)\alpha^2]\right)$$

$$J_n=\left(-\frac{1}{\Pr}\omega^2(n^2\pi^2+\alpha^2)^2+(n^2\pi^2+\alpha^2)^4-R_0\alpha^2[n^2\pi^2+(1+M_1)\alpha^2]\right)^2+\left(-\frac{\omega}{\Pr}(1+\Pr)(n^2\pi^2+\alpha^2)^3-C\omega(n^2\pi^2+\alpha^2)^4\right)^2 \qquad (17)$$

5. Results and Discussion

The purpose of the study is to investigate the impact of a time-dependent magnetic field on the advent of convection in a ferromagnetic liquid with couple stress effect. The values of the Rayleigh number as well as the associated wavenumber are calculated using the regular perturbation method. Magnetic modulation is assumed up to order of $O(\varepsilon^2)$ [31], emphasizing that the amplitude ε of the modulation is quite small. It is difficult to achieve the critical correction Rayleigh number R_{2c} expression without this assumption. M_1, *Pr* and *C* are the parameters that emerge in this study as being influenced by modulation frequency ω. The stabilizing impact of modulation is indicated by a positive R_{2c}, while the destabilizing impact of modulation is indicated by a negative R_{2c}. The fixed values of the parameters M_1=25, *Pr*=5 and *C*=0.1 are used in the study at hand. The results are visually described in figures 2 through 4 to gain a thorough understanding of the physical situation, we find from these figures that the value of $R_{2c}>0$ in all the cases. As a result, magnetic field modulation has a stabilizing effect on the system in the presence of both magnetization and couple stresses, with convection occurring at a later point than in the unmodulated system.

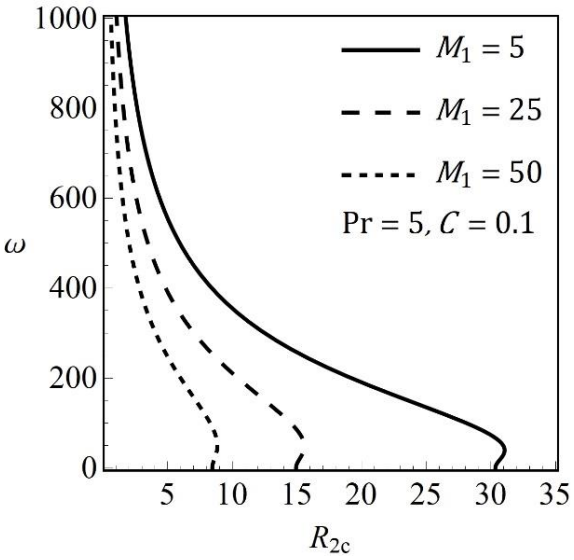

Fig. (2) Variation of R_{2c} with respect to ω for different values of M_1

Figure (2) illustrates the effect of the buoyancy magnetization parameter M_1 over the variation of critical correction Rayleigh number R_{2c} with frequency ω. It is observed from this figure that if ω is small, the value of R_{2c} is let down by increasing the quantity of M_1. For moderate and high values of ω, R_{2c} shows the equivalent impact on the system, indicating that the effect of magnetic mechanism M_1 is to diminish the stabilizing effect on the magnetic field modulated fluid layer.

 © ALL RIGHTS RESERVED

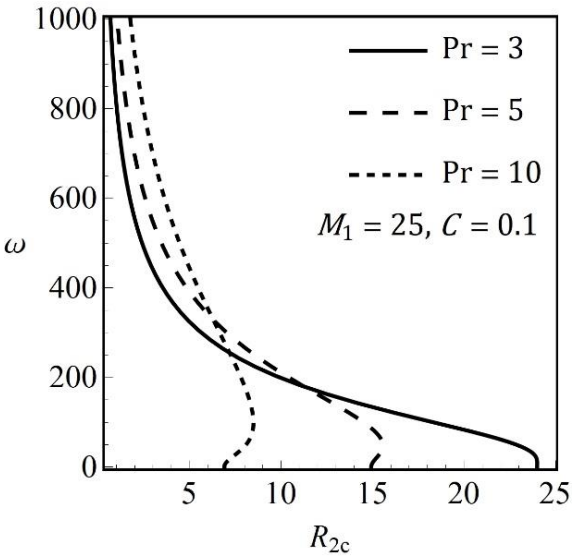

Fig. (3) Variation of R_{2c} with respect to ω for different values of Pr

In Fig. (3), we address the effect of the Prandtl number Pr on R_{2c}. As long as ω is small, R_{2c} decreases as Pr increases. However, if ω is intermediate and big, the pattern reverses. Furthermore, the Prandtl number mitigates the effects of magnetic field variations. In addition, if ω is small enough, the significant influence of Pr on stability is demonstrated.

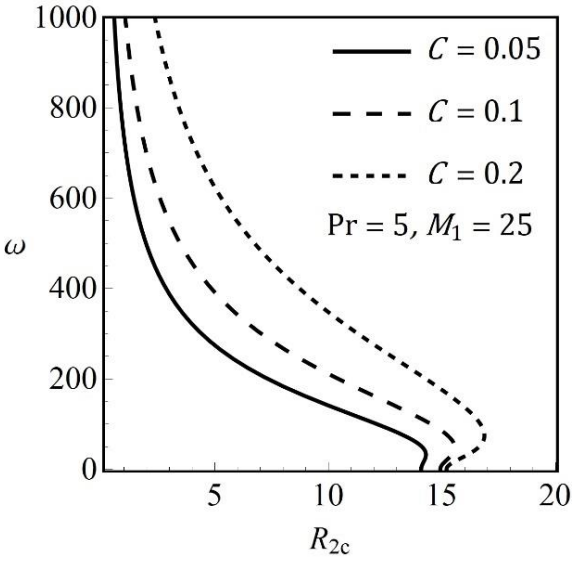

Fig. (4) Variation of R_{2c} with respect to ω for different values of C

Figure (4) represents the effect of couple stress parameter C on the critical correction Rayleigh number R_{2c} with frequency ω by fixing other parameters. We observe from this graph that as C increases the value of critical correction Rayleigh number R_{2c} increases over entire range of values of ω indicating that the effect of couple stress is to stabilize the system.

6. Conclusions

On the basis of Stokes micro-continuum theory, the combined effect of couple stresses signifying non-Newtonian characteristics of the ferrofluid and magnetic modulation heated from below is examined. The central conclusions of the present study are the following. The buoyancy magnetization parameter M_1 reduces the stabilizing effect of magnetic field modulation. The couple stress parameter C has a stabilizing effect on the system. The Prandtl number Pr has destabilizing effect on the system provided ω is small while the opposite effect is seen for moderate and large value of ω. From figures (2-4), $R_{2c}>0$ in all the cases indicating that magnetic field modulation has a stabilizing effect on the system in the presence of both magnetization and couple stresses. Effects of M_1, Pr, C and modulation on magnetic force disappear when the frequency of magnetic modulation is considerably large.

References

[1] J. Popplewell, "Technological applications of ferrofluids", *Phys. Technol.*, 15(3) (1984) 150-156.

[2] B.M. Berkovsky, V.F. Medvedev and M.S. Krakov, **"Magnetic fluids: engineering applications"**, Oxford: Oxford Science Publications (1993).

[3] H.E. Horng et al., "Novel properties and applications in magnetic fluids", *J. Phys. Chem. Solids.*, 62(9-10) (2001) 1749-1764.

[4] B. A. Finlayson, "Convective instability of ferromagnetic fluids", *J. Fluid Mech.*, 40(4) (1970) 753-767.

[5] M. Das Gupta and A.S. Gupta, "Convective instability of a layer of a ferromagnetic fluid rotating about a vertical axis", *Int. J. Eng. Sci.*, 17(3) (1979) 271-277.

[6] K. Gotoh and M. Yamada, "Thermal convection in a horizontal layer of magnetic fluids", *J. Phys. Soc. Japan.*, 51(9) (1982) 3042-3048.

[7] P.J. Stiles, F. Lin and P.J. Blennerhassett, "Heat transfer through weakly magnetized ferrofluids", *J. Colloid Interface Sci.*, 151(1) (1992) 95-101.

[8] S. Maruthamanikandan, "Effect of radiation on Rayleigh-Bénard convection in ferromagnetic fluids", *Int. J. Appl. Mech. Eng.*, 8(3) (2003) 449-459.

[9] S. Mathew and S. Maruthamanikandan, "Darcy-Brinkman Ferro convection with temperature dependent viscosity", *J. Phys. Conf. Ser.*, 1139(1) (2018) 012023.

[10] S. Maruthamanikandan, N. Mary Thomas and S. Mathew, "Thermorheological and magnetorheological effects on Marangoni-Ferroconvection with internal heat generation", *J. Phys. Conf. Ser.*, 1139(1) (2018) 012024.

[11] V. Vidya Shree et al., "Effect of MFD viscosity

on ferroconvection in a fluid saturated porous medium with variable gravity", *J. Mines Met. Fuels.*, 70(3A) (2022) 98-108.
[12] S. Aniss, M. Belhaq and M. Souhar, "Effects of a magnetic modulation on the stability of a magnetic liquid layer heated from above", *J. Heat Transfer.*, 123(3) (2001) 428-433.
[13] P.N. Kaloni and J.X. Lou, "Convective instability of magnetic fluids under alternating magnetic fields", *Phys. Rev. E - Stat. Nonlinear, Soft Matter Phys.*, 71(6) (2005) 1-12.
[14] P. Matura and M. Lücke, "Thermomagnetic convection in a ferrofluid layer exposed to a time-periodic magnetic field", *Phys. Rev. E - Stat. Nonlinear, Soft Matter Phys.*, 80(2) (2009) 1-9.
[15] H. Engler and S. Odenbach, "Thermomagnetic convection in magnetic fluids influenced by a time-modulated magnetic field", *Proc. Appl. Math. Mech.*, 8(1) (2008) 10951-10952.
[16] H. Engler and S. Odenbach, "Influence of parametric modulation on the onset of thermomagnetic convection", *Proc. Appl. Math. Mech.*, 9(1) (2009) 515-516.
[17] O. P. Keshri, A. Kumar and V. K. Gupta, "Effect of internal heat source on magneto-stationary convection of couple stress fluid under magnetic field modulation", *Chinese J. Phys.*, 57(1) (2019) 105-115.
[18] C. Balaji et al., "Ferroconvection in a sparsely distributed porous medium with time-dependent sinusoidal magnetic field", *J. Mines Met. Fuels.*, 70(3A) (2022) 28-34.
[19] V. K. Stokes, "Couple stresses in fluids", *Phys. Fluids.*, 9(9) (1966) 1709-1715.
[20] V.K. Stokes, **"Theories of Fluids with Microstructure: An Introduction"**, Springer Berlin Heidelberg (1984) 150-178.
[21] L.M. Srivastava, "Peristaltic transport of a couple-stress fluid", *Rheol. Acta.*, 25(6) (1986) 638-641.
[22] J.R. Lin, "Effects of couple stresses on the lubrication of finite journal bearings", *Wear*, 206(1-2) (1997) 171-178.
[23] R.C. Sharma, "Effect of suspended particles on couple-stress fluid heated from below in the presence of rotation and magnetic field", *Ind. J. Pure Appl. Math.*, 35 (2004) 973-989.
[24] M.S. Malashetty and P. Kollur, "The onset of double diffusive convection in a couple stress fluid saturated anisotropic porous layer", *Transp. porous media.*, 86(2) (2011) 435-459.
[25] S. Saravanan and D. Premalatha, "Effect of couple stress on the onset of thermovibrational convection in a porous medium", *Int. J. Therm. Sci.*, 57 (2012) 71-77.
[26] Mubeen Taj, S. Maruthamanikandan and S. K. Akbar, "Effect of Chemical Reaction on Convective Instability in a Horizontal Porous Layer Saturated with a Couple-Stress Fluid", *Int. J. Eng. Res. Appl.*, 3(2) (2013) 1742-1748.
[27] A. Kumar, Vanita and V.K. Gupta, "Study of heat and mass transport in Couple-Stress liquid under G-jitter effect", *Ain Shams Eng. J.*, 9(4) (2018) 973-984.
[28] M. Rudziva et al., "A numerical study of heat and mass transfer in a Darcy porous medium saturated with a couple stress fluid under rotational modulation", *Appl. Math. Model.*, 104 (2022) 455-473.
[29] N.M. Thomas and S. Maruthamanikandan, "Effect of gravity modulation on the onset of ferroconvection in a densely packed porous layer", *IOSR J Appl Phys*, 3 (2013) 30-40.
[30] S. Chandrasekhar, **"Hydrodynamic and Hydromagnetic Stability"**, Clarendon Press: Oxford University Press, (1961).
[31] G. Venezian, "Effect of modulation on the onset of thermal convection", *J. Fluid Mech.*, 35(2) (1969) 243-254.
[32] N.M. Thomas and S. Maruthamanikandan, "Gravity modulation effect on ferromagnetic convection in a Darcy-Brinkman layer of porous medium," *J. Phys. Conf. Ser.*, 1139(1) (2018) 012022.

 © ALL RIGHTS RESERVED

The Nobel Prize in Physics 2022

The Royal Swedish Academy of Sciences has decided to award the Nobel Prize in Physics 2022 to

Alain Aspect
Institut d'Optique Graduate School – Université Paris-Saclay and École Polytechnique, Palaiseau, France

John F. Clauser
J.F. Clauser & Assoc., Walnut Creek, CA, USA

Anton Zeilinger
University of Vienna, Austria

"for experiments with entangled photons, establishing the violation of Bell inequalities and pioneering quantum information science"

Entangled states – from theory to technology

Alain Aspect, John Clauser and Anton Zeilinger have each conducted groundbreaking experiments using entangled quantum states, where two particles behave like a single unit even when they are separated. Their results have cleared the way for new technology based upon quantum information.

The ineffable effects of quantum mechanics are starting to find applications. There is now a large field of research that includes quantum computers, quantum networks and secure quantum encrypted communication.

One key factor in this development is how quantum mechanics allows two or more particles to exist in what is called an entangled state. What happens to one of the particles in an entangled pair determines what happens to the other particle, even if they are far apart.

For a long time, the question was whether the correlation was because the particles in an entangled pair contained hidden variables, instructions that tell them which result they should give in an experiment. In the 1960s, John Stewart Bell developed the mathematical inequality that is named after him. This states that if there are hidden variables, the correlation between the results of a large number of measurements will never exceed a certain value. However, quantum mechanics predicts that a certain type of experiment will violate Bell's inequality, thus resulting in a stronger correlation than would otherwise be possible.

John Clauser developed John Bell's ideas, leading to a practical experiment. When he took the measurements, they supported quantum mechanics by clearly violating a Bell inequality. This means that quantum mechanics cannot be replaced by a theory that uses hidden variables.

Some loopholes remained after John Clauser's experiment. **Alain Aspect** developed the setup, using it in a way that closed an important loophole. He was able to switch the measurement settings after an entangled pair had left its source, so the setting that existed when they were emitted could not affect the result.

Using refined tools and long series of experiments, **Anton Zeilinger** started to use entangled quantum states. Among other things, his research group has demonstrated a phenomenon called quantum teleportation, which makes it possible to move a quantum state from one particle to one at a distance.

"It has become increasingly clear that a new kind of quantum technology is emerging. We can see that the laureates' work with entangled states is of great importance, even beyond the fundamental questions about the interpretation of quantum mechanics," says Anders Irbäck, Chair of the Nobel Committee for Physics.

Alain Aspect, born 1947 in Agen, France. PhD 1983 from Paris-Sud University, Orsay, France. Professor at Institut d'Optique Graduate School – Université Paris-Saclay and École Polytechnique, Palaiseau, France.

John F. Clauser, born 1942 in Pasadena, CA, USA. PhD 1969 from Columbia University, New York, USA. Research Physicist, J.F. Clauser & Assoc., Walnut Creek, CA, USA.

Anton Zeilinger, born 1945 in Ried im Innkreis, Austria. PhD 1971 from University of Vienna, Austria. Professor at University of Vienna, Austria.

Prize amount: 10 million Swedish kronor, to be shared equally between the laureates.
Further information: www.kva.se and www.nobelprize.org
Press contact: Eva Nevelius, Press Secretary, +46 70 878 67 63, eva.nevelius@kva.se
Experts: Thors Hans Hansson, +46 70 376 89 63, hansson@fysik.su.se and Mats Larsson, +46 73 389 43 77, ml@fysik.su.se, members of the Nobel Committee for Physics.

The Royal Swedish Academy of Sciences, founded in 1739, is an independent organisation whose overall objective is to promote the sciences and strengthen their influence in society. The Academy takes special responsibility for the natural sciences and mathematics, but endeavours to promote the exchange of ideas between various disciplines.

Nobel Prize® is a registered trademark of the Nobel Foundation.

IRAQI JOURNAL OF APPLIED PHYSICS
Vol. 18, No. 4, October-December 2022, pp. 21-25

Spectroscopic Study of Sol-gel Synthesized Silica Xerogel Embedded with Dysprosium Ions

Amenah A. Salman[1]
Firas J. Al-Maliki[2]

[1] *Department of Communication Engineering, University of Technology, Baghdad, IRAQ*
[2] *Department of Physics, College of Science, University of Baghdad, Baghdad, IRAQ*

Recently, Dysprosium Dy^{3+} ions embedded in silica xerogels have been synthesized and investigated as a function of Dy^{3+} concentrations. The spectroscopic activity of Dy^{+3} ions in silica matrix has been observed through recording the absorption and luminescence spectra. The UV-Visible-NIR spectra revealed absorption peaks due to Dy^{3+} active centers. The $^4F_{9/2}$ emissions have been observed from a minority of isolated Dy^{3+} ions within the pores structure of silica matrix, and the FTIR result supports the distribution of such ions in these porous. The analysis indicates that at doping levels, most ions reside in clusters and $^4F_{9/2}$ emission, which is demonstrated by the quenching observed in the corresponding spectra. Some spectroscopic parameters such as emission cross-section σ_{em} and oscillator strength f_{exp} have been determined and analyzed.

Keywords: Lanthanide; Luminescence quenching; Sol-gel; Spectroscopic parameters
Received: 26 July 2022; **Revised:** 17 September 2022; **Accepted:** 24 September 2022

1. Introduction

Spectroscopy of lanthanide ions integrated into host glasses are used extensively in different scientific and technical applications such as optical amplifiers, bar-code reading, optical fibers, optical detector, optical communication, optical data storage devices, and solid-state materials emitting visible light (near white light emitting diode LEDs) due to 4f–4f and 4f–5d electronic transitions [1]. White light-emitting diodes (W-LEDs) generate white light using phosphors and a short-wavelength excitation source in the visible and ultraviolet spectral regimes. They now play an essential role in modern lighting due to their high efficiency, relatively low cost, compact structure, and simple driving circuitry [2].

In developing lanthanide doped optical devices, the selection of host glass matrix is significant because the spectral transitions of lanthanide ions are host-dependent [1-2]. The spectroscopic properties of lanthanide ions depend on their 4f–4f transitions and can be controlled by changing the chemical composition of the host glass matrix [3]. Among lanthanide ions, the Dy^{3+} ($^4F^9$) ion is one of the best suitable candidates for preparing visible lasers and phosphor materials. Depending on the host, It can emit several attractive visible wavelengths between its f–f transitions. The Dy^{3+} ion is one of the most studied lanthanide ions. Special attention has recently been on studying Dy^{3+}-doped glass due to its protentional applications for high-density optical storage, undersea communication, and color display [4]. The visible fluorescence of Dy^{3+} ion contains two intense bands, one in blue (470-500 nm) and the other one in yellow (570-600 nm) regions, which are due to the transitions $^4F_{9/2}\rightarrow{}^6H_{15/2}$ and $^4F_{9/2}\rightarrow{}^6H_{13/2}$, respectively [4-5].

Lanthanide-doped silica can be made in bulk by any of several methods, including high-temperature vapor phase processing, [6] sol-gel chemistry [7-9], or ion implantation [10]. The sol-gel processing emerged as an attractive alternative for the fabrication of glasses utilizing combinations of II-VI semiconductors, Lanthanides and dielectrics like SiO_2. Silica prepared by sol-gel is environmentally friendly and has good thermal and chemical stability. This method can provide suitable host material via the transition states of viscous gels produced by polymerization metal alkoxides [11].

In the present work, we have focused our attention on the spectroscopic parameters and properties of silica xerogel doped with Dy^{3+} to obtain more information about the nature of lanthanides as phosphor materials emitting visible light.

2. Experimental Part

Sol-gel synthesized undoped silica xerogel, and Dy^{3+}-doped silica xerogel was used to prepare bulk samples as a function of Dy^{3+} ion concentration described in Fig. (1). Tetraethyl orthosilicate (TEOS, purity >98% supplied by Schuchardt, Germany), ethanol (C_2H_5OH, 99.0% supplied by Fluka Garantie, Germany), and water were used as starting materials, and hydrochloric acid (HCl) was used as the catalyst. The molar ratio was taken as 1:5:10 for TEOS/ethanol/water. Dysprosium chloride hexahydrate ($DyCl_3.6H_2O$, 99.9 % from Aldrich) was used as the source of Dy^{3+} ions. All samples were prepared by first dissolving TEOS in ethanol by magnetic stirring for 30 min. Then dilute HCl was

 © ALL RIGHTS RESERVED

added to the solution instead of pure water to catalyze the hydrolysis/condensation reaction. The mixture was stirred continuously for another 30 min. A different concentration of Dy^{3+} solutions was prepared by dissolved $DyCl_3.6H_2O$ in deionized water; 1 ml of these solutions with different concentrations (1, 0.55, 0.35, 0.2, 0.125) $x10^{-1}$ M was added to the mixture and stirred for 30 min to produce the samples. All solutions are left for the aging process for 12 hours. A gel was produced when storing the solutions in closed containers placed in an oven at 60 °C, and then the first gel drying occurred at a temperature of 60 °C in open containers for 24 hours to achieve a transparent sample. Finally, the drying process was done to let the solvent evaporation from samples in an oven at 90-110 °C for 48 hours with the range 5 °C every 12 hours.

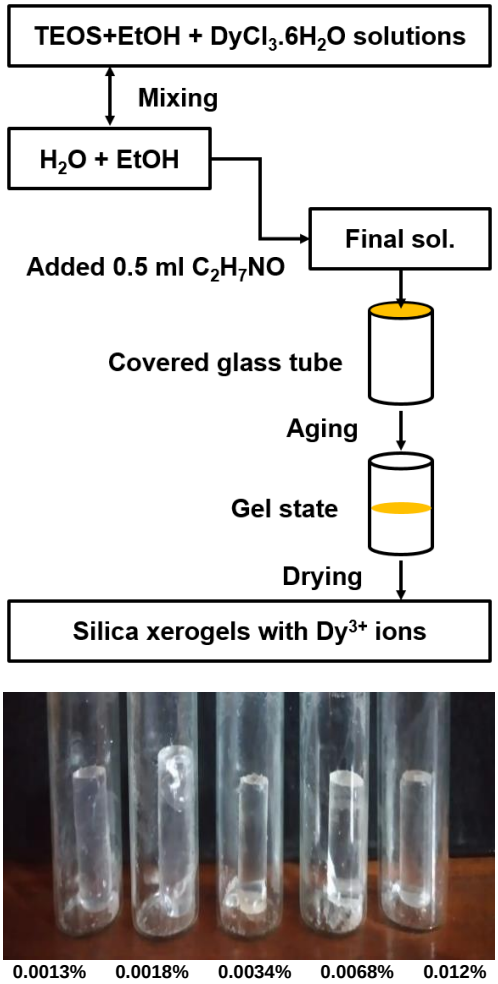

Fig. (1) Sol-gel preparation scheme for Dysprosium-doped silica xerogels

3. Results and Discussion

Figure (2) shows the absorption spectra of Dy^{3+} solutions were recorded using a Shimadzu UV-1800 Double-Beam UV-Visible spectrophotometer. Eight absorption bands caused by electronic transitions of an energy level of Dy^{3+} ions are recorded, and the wavelengths to these bands are equal to about 324, 350, 365, 388, 453, 760, 808 and 911 nm due to the transition $^6H_{15/2} \rightarrow {}^6P_{3/2}$, $^6P_{7/2}$, $^6P_{5/2}$, $^4I_{13/2}$, $^4I_{15/2}$, $^6F_{3/2}$, $^6F_{5/2}$ and $^6F_{7/2}$ levels, respectively [11-12]. The absorbance that corresponds to these transitions depends on the concentration of the Dy^{3+} ions in the solutions; when the concentration of Dy^{3+} increases, the absorbance becomes increasingly prominent and sharper, and this is due to the increase of ions contribution in the absorption process so much as the increase of their concentrations according to Lambert–Beer's law.

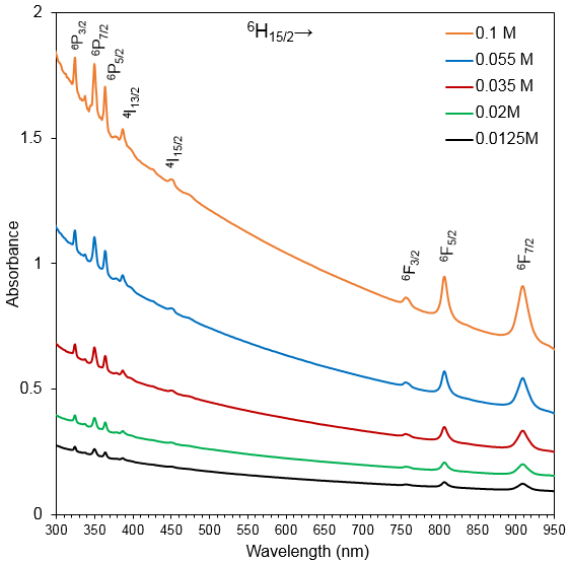

Fig. (2) Absorption spectra of Dy^{3+} ions in the solutions

The absorption spectra presented in Fig. (3) for the doped samples (0.00135-0.012%) show absorption bands corresponding to intraconfigurational $4f^n$-$4f^n$ transitions of the Dy^{3+} ions. These transitions suggest that the spectroscopic activity of the ions in samples and solutions is the same, and absorbance increases with increasing concentrations of Dy^{3+} ions with a slight blue shift. According to published information, each transition's shape and peak position are the same as the other samples. [12-14].

Figure (4) illustrates the recorded photoluminescence spectra using the 350 nm excitation wavelength of the xenon lamp source (Shimadzu RF-5301 PC Spectrofluorophotometer). The emission band at 575 nm is attributed to the transition: $^4F_{9/2} \rightarrow {}^6H_{13/2}$. The hypersensitive 575nm yellow-region emission is well known to correspond to the induced electric dipole transition, which is strongly influenced by the host environment [14-16]. It is worth observing that the emission intensity is higher in the sample with a concentration of 0.0034 mol.% than in the other samples. Their occurrences of luminescence quenching for Dy^{3+} in the silica matrix that were observed in other concentrations could be due to the energy transfer among the excited Dy^{3+} ions, such as the interaction between the

lanthanide ions due to cross-relaxation (CR), strong interaction between two active ions can transfer the excitation energy from Dy^{3+} ion to another, O-H vibrations of water and concentration quenching exhibited by Dy^{3+} ions at higher concentrations. This phenomenon is most likely caused by the increase in the number of nonradiative decay channels and also due to many closely spaced excited states, which leads to the quenching [17,18]; it indicates the clustering of these ions in the porous structures of sol-gel material.

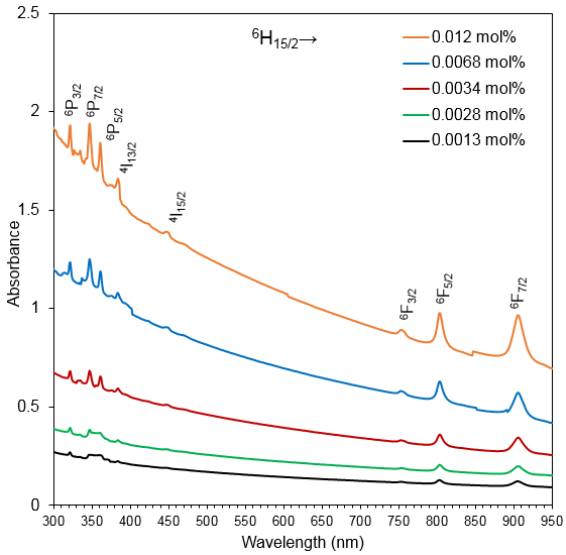

Fig. (3) Absorption spectra of silica xerogels doped with different concentrations of Dy^{3+} ions

The Fourier-transform infrared (FTIR) spectra recorded using Shimadzu FTIR spectrometer on KBr pellets of the samples over the range 4000-400 cm^{-1} of undoped and doped silica samples are illustrated in Fig. (5). They supported the distribution of ions in these porous structures. The characteristics vibrational bands of the host contain five absorption bands were found at about 470, 800 and 1064 cm^{-1}, which were due to bending, symmetric stretching, and asymmetric stretching vibrations of Si-O-Si groups respectively, while the weak band at about 960 cm^{-1} was due to stretching vibration of Si-OH groups. Another two bands appeared at about 1658 and 3419 cm^{-1}, which are characteristic of vibration of the O-H bond in water molecules [19,20], indicating that the drying process at 60 °C does not completely trap the water molecules from the silica pores.

The spectroscopic parameters, such as absorption coefficients α(λ) and absorption cross-sections σ(λ), can be calculated from absorption spectra using the formula [21]:

$$\sigma(\lambda) = \frac{\alpha(\lambda)}{\rho} \qquad (1)$$

where ρ is the ion density (cm^{-3}), the refractive index n(λ) calculated by Michelson interferometer was about 1.46-1.47. Bowen and Wokes gave an empirical formula to get a sufficiently accurate value of radiative lifetime (τ_{rad}) [22]:

$$\frac{1}{\tau_{rad}} = 2.88 \times 10^{-9} \times n^2 \times \dot{\upsilon} \int \varepsilon(\dot{\upsilon}) d\dot{\upsilon} \qquad (2)$$

where $\dot{\upsilon}$ is the wavenumber at the peak of the absorption band (in cm^{-1}) and $\int \varepsilon(\dot{\upsilon}) d\dot{\upsilon}$ is the area under the absorption band curve, and $\varepsilon(\dot{\upsilon})$ is the molecular extinction coefficient

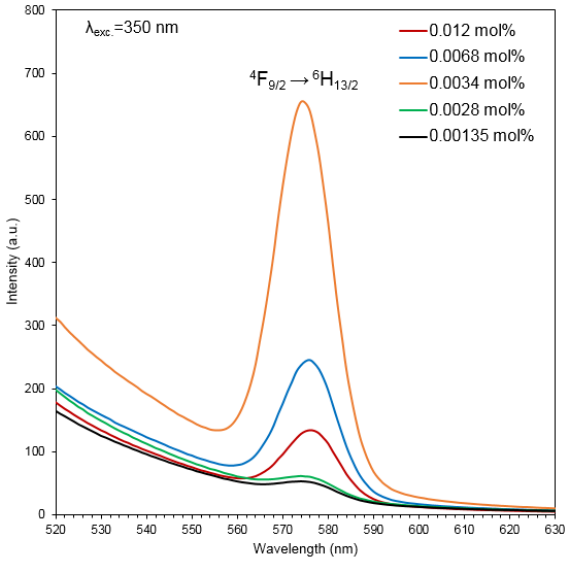

Fig. (4) Emission spectra of silica xerogel doped with Dy^{3+} ions excited by 350 nm

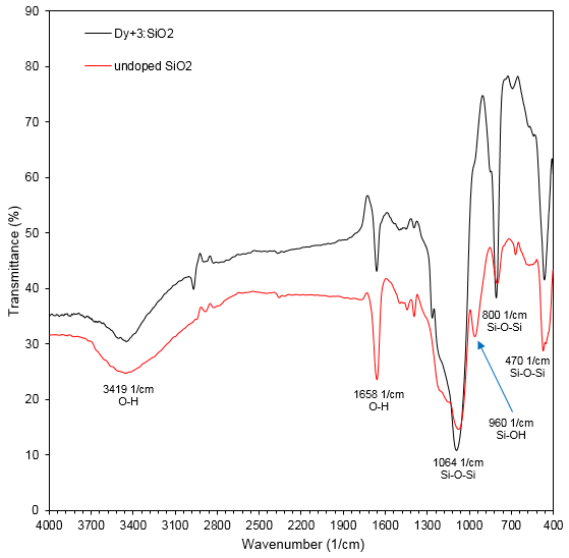

Fig. (5) FTIR spectra of undoped silica xerogel and Dy^{3+}-doped silica xerogel

The peak emission cross-section (σ_{em}) for transition $^4F_{9/2} \rightarrow {}^6H_{13/2}$ can determined from:

$$\sigma_{em} = \frac{\lambda p^4}{8\pi\, c\, n'^2\, \Delta\lambda_{eff}\, \tau_{rad}} \qquad (3)$$

where λ_p is the peak wavelength within the fluorescence band, $\Delta\lambda_{eff}$ is the emission linewidth (effective); which is determined by the full-width at

 © ALL RIGHTS RESERVED

half maximum (FWHM) of the emission band, and ń is given by:

$$n' = \frac{(n^2(\lambda)+2)^2}{9n(\lambda)} \quad (4)$$

The oscillator strength (f_{exp}) can be calculated from the absorption spectra using the formula [23]:

$$f_{exp} = 4.32 \times 10^{-9} \int \varepsilon(\grave{\upsilon})d\grave{\upsilon} \quad (5)$$

Table (1) shows the results of the calculated parameters from the recorded spectra. These parameters are related to the absorption band for transition $^6H_{15/2} \rightarrow {}^6P_{7/2}$ and the emission band for transition $^4F_{9/2} \rightarrow {}^6H_{13/2}$ of Dy^{3+} ions. Figure (6) displays the behavior of the oscillator strength (f_{exp}) and peak emission cross-section (σ_{em}) with different concentrations of Dy^{3+} ions in the doped samples. This figure also shows that the f_{exp} and σ_{em} are slightly increasing with an increase in the Dy^{3+} ions concentration to reach a maximum value of 0.0034 mol.% and then slightly decreasing with increasing concentration. This behavior is caused by the luminescence quenching effect. The oscillator strength values of Dy^{3+} are connected with hypersensitive electric dipole transitions and indicate a non-symmetrical surrounding of Dy^{3+} ions in the silica network.

Table (1) Spectroscopic parameters of silica xerogel doped with Dy^{3+} ions

Sample no.	Dy^{3+} ions Concentration (%)	Absorption cross-section $\sigma(\lambda)$ ($x10^{-19}$ cm^2)	Radiative lifetime τ_{rad} (ms)	Oscillator Strength f_{exp} ($x10^{-6}$)	Emission Cross section σ_{em} ($x10^{-19}$ cm^2)
SDy1	0.0013	0.9	1.1	0.82	0.24
SDy2	0.0028	0.82	0.98	0.86	0.26
SDy3	0.0034	0.93	0.51	1.65	0.37
SDy4	0.0068	1.08	0.57	1.47	0.33
SDy5	0.012	9.3	0.62	1.36	0.32

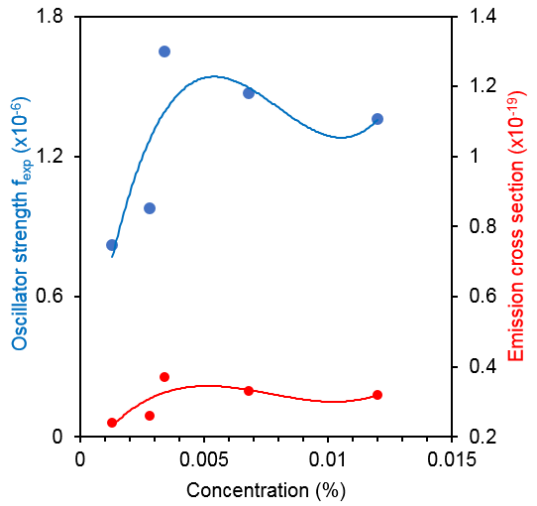

Fig. (6) Variation in oscillator strength (f_{exp}) and peak emission cross-section (σ_{em}) with the concentrations of Dy^{3+} ions in doped samples

4. Conclusions

The sol-gel method was successfully used to synthesize transparent silica xerogels and silica xerogels containing up to 0.012 mol.% of Dy^{3+} ions. The structural behavior of these ions in these matrices is described as randomly dispersed and unable to form any ligands in silica networks. These ions emit intense visible radiation and the spectroscopic characterization shows that the Dy^{3+} ions are clumped within the pores of the silica sol-gel host, suppressing emission at high doping levels. The present results are considered a promising start for future research into the possibility of enhancing the visible emissions of such ions by co-doping with metal nanoparticles like silver and gold that are advantageous in white light-emitting diode (W-LED) applications.

References

[1] D.D. Ramteke and R.S. Gedam, "Study of Li_2O–B_2O_3–Dy_2O_3 glasses by impedance spectroscopy", *Solid State Ion.*, 258 (2014) 82-87.

[2] M. Peysokhan et al., "Implementation of Laser-Induced Anti-Stokes Fluorescence Power Cooling of Ytterbium-Doped Silica Glass", *ACS Omega*, 6(12) (2021) 8376-8381.

[3] C. Racles, A. Nistor and M. Cazacu, "A Silica-Silver Nanocomposite Obtained by Sol-Gel Method in the Presence of Silver Nanoparticles", *Cent. Eur. J. Chem.*, 11(10) (2013) 1689-1698.

[4] C. Zhu et al., "Excitability of High-Energy Ultraviolet Radiation for Dy^{3+} in Antimony Phosphate Glasses", *Mater. Sci. Poland*, 35(2) (2017) 346-354.

[5] P. Paradis et al., "Dysprosium-Doped Silica Fiber as Saturable Absorber for Mid-Infrared Pulsed All-Fiber Lasers", *Opt. Exp.*, 30(3) (2022) 3367-3378.

[6] Sk. Mahamuda et al., "Lasing Potentialities and White Light Generation Capabilities of Dy^{3+} Doped Oxy-Fluoroborate Glasses", *J. Lumin.*, 153 (2014) 382-392.

[7] A.N. Gusev et al., "Synthesis, Structure and Luminescence Studies of Eu(Iii), Tb(Iii), Sm(Iii), Dy(Iii) Cationic Complexes with Acetylacetone Andbis(5-(Pyridine-2-Yl)-1,2,4-Triazol-3-Yl)Propane", *Inorg. Chim. Acta*, 406 (2013) 279-284.

[8] L.J. Dih et al., "Influence of Precursor Bi^{3+}/Fe^{3+} Ion Concentration on Hydrothermal Synthesis of $BiFeO_3$ Crystallites", *Ceram. Int.*, 40(3) (2014) 4575-4578.

[9] G.M. Taha et al., "Effect of Preheating Temperature on Synthesis of Pure $BiFeO_3$ via Sol-Gel Method", *Nanopages*, (2019) 1-11.

[10] A. Fet, V. Häublein, and A.J. Bauer, "Effective work function engineering by lanthanide ion implantation of metal-oxide semiconductor gate stacks", *J. Vac. Sci. Technol. B: Microelectron.*

Nanometer Struct. Process. Measur. Phen., 27 (2009) 290.

[11] F.T. Aquino et al., "Broadband NIR emission in novel sol–gel Er^{3+}-doped SiO_2–Nb_2O_5 glass ceramic planar waveguides for photonic applications", *Opt. Mater.*, 35 (2013) 387-396.

[12] P. van Do, "Optical Properties and White Light Emission of Dy^{3+}-Doped Alumino Boro-tellurite Glasses", *VNU J. Sci.: Math. Phys.*, 35(4) (2019) 52-58.

[13] N. Sooraj Hussain et al., "Absorption and Emission Analysis of Re^{3+}(Sm^{3+} and Dy^{3+}): Lithium Boro Tellurite Glasses", *J. Nanosci. Nanotech.*, 8 (2008) 1-6.

[14] N. Shasmala and B. Karmakara, "White Light-Emitting Dy^{3+}-Doped Transparent Chloroborosilicate Glass: Synthesis and Optical Properties", *J. Asian Cer. Soc.*, 7(1) (2019) 42-52.

[15] K.V. Babu et al., "White Light Generation in Dy^{3+}-Doped Sodium Lead Alumino Borosilicate Glasses for W-LEDApplications", *J. Aircraft Spacecraft Technol.*, 4 (2020) 39-47.

[16] N. Jaidass et al., "Luminescence properties of Dy^{3+}-doped lithium zinc borosilicate glasses for photonic applications", *Heliyon*, 4 (2018) e00555.

[17] D.D. Ramteke et al., "Concentration Effect of Sm^{3+} Ions on Structural and Luminescence Properties of Lithium Borate Glasses", *Phys. Procedia*, 76 (2015) 25-30.

[18] L.V. Vu et al., "Synthesis and Optical Characterization of Samarium Doped Lanthanum Orthophosphate Nanowires", *Mater. Trans.*, 56(9) (2015) 1422-1424.

[19] K. Linganna, Ch. Srinivasa Rao and C.K. Jayasankar, "Optical Properties and Generation of White Light in Dy^{3+}-Doped Lead Phosphate Glasses", *J. Quant. Spec. Rad. Transfer*, 1(18) (2013) 40-48.

[20] W.A.A. Twej et al., "FTIR Measurements for Structural Probing of Rare earth Sol-Gel Silica Glass System Co-Doped With Al^{3+}", *IEEE Xplore*, 14 (2011) 6369-6375.

[21] G.C. Righini and M. Ferrari, "Photoluminescence of Rare-Earth-Doped Glasses", *Rivista Del Nuovo Cimento*, 28(12) (2005) 1-53.

[22] E.J. Bowen and F. Wokes, **"Fluorescence of Solution"**, Langmans Green and Co. (London, 1953).

[23] C.M. Reddy et al., "Optical Absorption and Photoluminescence Studies of Dy^{3+}:LCZSFB Glasses", *Phot. Lett. Poland*, 3(1) (2011) 32-34.

 © ALL RIGHTS RESERVED

TRANSFORMATIVE LEARNING CONFERENCE

"My colleagues and I have pushed for transformative learning without knowing what it was. After this conference, I feel that we are experts in this field."

2019 Attendee

13th Annual Transformative Learning Conference
MARCH 30-31, 2023, OKLAHOMA CITY, OK, USA

The Transformative Learning (TL) conference, hosted by the University of Central Oklahoma (UCO), focuses on the design, application, and measurement of TL for student learning. One of the most significant conferences on the implementation of TL in higher education, the gathering has become a nexus for practitioner conversations and networking. It melds outstanding presentations, workshops, posters, and discussions about TL in action with a good time in Oklahoma. Annual post-conference surveys consistently refer to the sense of community at the conference as one of its greatest strengths.

2023 Featured Speakers

Dr. Peter Doolittle of Virginia Tech
Dr. Christine Harrington of New Jersey City University

Pre-Conference

Wednesday, March 29, 2023, for institutions interested in a deeper dive into UCO's Student Transformative Learning Record (STLR) process and tools, which is a key means of operationalizing TL at UCO and other institutions around the U.S. and the world.

Venue

Delta Hotel-Marriot (currently Sheraton Hotel) at the Reed Conference Center, which is just 7 miles from downtown Oklahoma City's (OKC) lively Bricktown canal and entertainment quarter, the Boathouse District, and a wide variety of exquisite OKC restaurants.

For more information and the Call for Presentations,
please visit https://www.uco.edu/tlconference.
Presentation submissions are peer-reviewed.

IRAQI JOURNAL OF APPLIED PHYSICS
Vol. 18, No. 4, October-December 2022, pp. 27-30

Zahraa H. Zaidan[1]
Kasim H. Mahmood[1]
Oday A. Hammadi[2]

[1] *Department of Physics, College of Education for Pure Sciences, Tikrit University, Tikrit, IRAQ*
[2] *Department of Physics, College of Education, Al-Iraqia University, Baghdad, IRAQ*

Using Banana Peels for Green Synthesis of Mixed-Phase Titanium Dioxide Nanopowders

In this work, titanium dioxide (TiO_2) nanopowders were synthesized from the titanium isopropoxide and banana peels by the solvothermal method. The synthesized nanopowder was polycrystalline and containing both anatase and rutile phases of TiO_2, with minimum nanoparticle size of 25.41, and good structural purity, which was supported by the spectroscopic measurements. The proposed method can be described as low-cost, reliable and simple method to synthesize TiO_2 nanopowders for practical applications that require mass quantities of this material with sufficiently good characteristics.

Keywords: Titanium dioxide; Nanoparticles; Solvothermal method; Green synthesis
Received: 01 September 2022; **Revised:** 25 October 2022; **Accepted:** 01 November 2022

1. Introduction

The needs for antibacterial and antifungal nanopowders, such as titanium dioxide (TiO_2) in most recent biological, medical and environmental applications, the methods and techniques to prepare and synthesize such nanopowders have been drastically varied and developed. Some methods and techniques can exceptionally produce highly-pure nanopowders either using the top-down or bottom-up approaches [1,2]. However, the requirements of such methods and techniques are relatively costive and complex [3]. Furthermore, the quantities of the produced nanopowders are very little to be used for mass treatment applications such as antibacterial and antifungal processes, pigments and paintings, hydrophobic and smart windows [4-7]. Therefore, alternative methods and techniques those can produce larger quantities of nanopowders are explored, employed, developed and optimized. Amongst, the solvothermal method is one of the most economical and simplest [8].

The solvothermal method can be described as an effective route to prepare titanium dioxide nanopowders with reasonably good control of their shape, size, distribution and crystallinity [9]. Such control is carried out throughout the experimental parameters included in this method, mainly, properties of solvent and precursor of titanium, addition of surfactants, solution and/or reaction temperatures, and reaction time [9,10]. Using organic solvents, such as ethanol, in the solvothermal method most likely leads to produce titanium dioxide nanopowders without foreign anions because such organic solvents are characterized by low relative permittivity and lack to ionic species [1]. On the other hand, the titanium dioxide nanopowders produced by the solvothermal method, just like all methods and techniques containing chemical reactions in solutions, are most likely consisting of anatase and rutile phases of titanium dioxide [11]. Obviously, the structural phase that initially forms during the preparation of titanium dioxide is the anatase, which is metastable phase. Due to thermal effects, the anatase phase converts into rutile phase, which is stable. Consequently, the titanium dioxide sample is described as mixed-phase (anatase/rutile) [12,13]. In pure synthetic titanium dioxide, the anatase to rutile phase transition usually occurs at temperature range of 600-700 °C. This transition temperature can be altered by various methods, including modifying the precursor or by adding dopant or modifier to the TiO_2 sample [14]. Despite that the environment, solution and reaction temperatures do not exceed 100 °C, the transition may occur locally as the TiO_2 particles are grown at the nanoscale [15]. As the intended applications of titanium dioxide nanopowders are not highly sensitive to the structural phase of these nanopowders, a low-cost, reliable, reasonably simple method such as solvothermal method is highly preferred [16].

In this work, mixed-phase titanium dioxide nanopowders were synthesized by a green route using titanium isopropoxide as a precursor and banana peels. The characteristics of the synthesized nanopowders were introduced.

2. Experimental Work

Fresh banana fingers from the local market were used to obtain the peels before wilt. These peels were cut into small pieces, washed three times with distilled water to remove any contaminants and dirt, and dried with drying paper. Then, 75 g of the dried peels were put in a beaker containing 150 mL of distilled water. The mixture was heated up to boiling temperature (100 °C) for 20 min. Then, the boiled mixture was filtered twice using Whatman No. 1 filter paper. The extracted solution was kept in the freezer at (≤4 °C).

An aqueous solution was prepared by solving 100 mg of titanium isoprpoxide ($C_{12}H_{28}O_4Ti$) in 1 mL of

 © ALL RIGHTS RESERVED

distilled water. The extracted solution of banana peels was taken out from the freezer and heated up to 60 °C for 10 min. A 50 mL of the extracted solution was drawn and put in a beaker on a magnetic hot plate stirrer. Then, 5 mL of the aqueous solution of $C_{12}H_{28}O_4Ti$ was taken and added to the 50 mL of extracted solution as drops while keeping stirring for one hour. The mixture was filtered using Whatman No. 1 filter paper to separate the formed nanopowder. These filtered nanopowder were washed twice with distilled water to remove any residuals from the previous mixing process and reaction step. The separated nanopowder was dried by heating up to 100 °C for 24 hours and then kept in sealed container to be characterized and then used in the intended applications.

The structural characteristics of the synthesized nanopowders were determined by x-ray diffraction (XRD) patterns using a Bruker D2 PHASER XRD system (Cu-Kα x-ray tube with λ=1.54056Å), the surface morphology was determined by an Inspect F50 field-emission scanning electron microscope (FE-SEM) using , the elemental constitution was determined by energy dispersive x-ray spectroscopy (EDX), the formation of molecular bonds and their vibrations were determined by Fourier-transform infrared (FTIR) spectroscopy using a SHIMADZU FTIR-8400S instrument, and the absorption spectra were recorded using a K-MAC SpectraAcademy SV-2100 spectrophotometer in the range of 300-800 nm as the synthesized nanopowder was immersed in a transparent viscous host as a reference.

3. Results and Discussion

Figure (1) shows the XRD pattern of the TiO_2 nanopowder synthesized in this work. Obviously, 14 peaks are seen, which belong all to the TiO_2; 8 of them for anatase (A) phase and 6 for rutile (R) phase. This is why the TiO_2 nanopowder referred to as mixed-phase and polycrystalline [17]. The formation of rutile phase cannot be avoided even much more care is considered during the formation of nanopowder as heating steps are necessarily required.

The crystallite size (D) was determined for all peaks, as shown in table (1), by Scherrer's equation as [18]:

$$D = \frac{0.9\lambda}{\beta cos\theta} \qquad (1)$$

where λ is the wavelength of x-rays (1.54Å), 0.9 is a constant, β is the full width at half-maximum (FWHM), which was given by the software of the XRD instrument

Figure (2) shows the FE-SEM image of the TiO_2 nanopowder synthesized in this work. It is clear that the TiO_2 nanoparticles in the nanopowder sample have different sizes with a minimum size of 25.41 nm, however, the differences are not high enough to consider this sample is inhomogeneous. As well, aggregation is apparent, which is unavoidable in any preparation method or technique that includes formation processes based on thermally-activated chemical reactions [19].

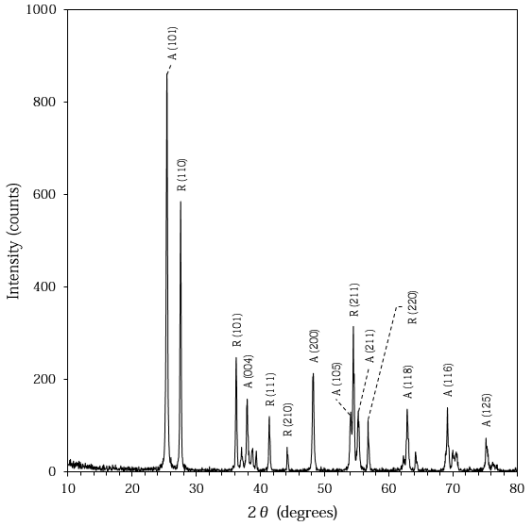

Fig. (1) XRD pattern of synthesized TiO_2 nanopowder

Table (1) Determination of crystallite size for the synthesized mixed-phase TiO_2 nanopowder

Peak no.	2θ (deg)	D (nm)	Phase	(hkl)
1	25.44	13.227	A	(101)
2	27.6	14.722	R	(110)
3	36.24	14.770	R	(101)
4	37.92	15.388	A	(004)
5	41.36	13.537	R	(111)
6	44.16	11.686	R	(210)
7	48.24	14.765	A	(200)
8	54.04	15.858	A	(105)
9	54.48	14.780	R	(211)
10	55.24	15.944	A	(211)
11	56.76	10.482	R	(220)
12	62.88	15.298	A	(118)
13	69.12	17.501	A	(116)
14	75.12	20.497	A	(125)

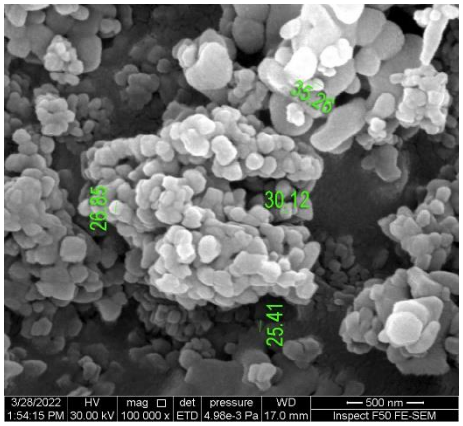

Fig. (2) FE-SEM image of synthesized TiO_2 nanopowder

Figure (3) shows the EDX results of the TiO_2 nanopowder synthesized in this work. The color mapping images (Fig. 3a) show that the volume density of Ti atoms is higher than that of O, which is confirmed by the elemental weight analysis (73.1% Ti vs. 26.8% O). This may be attributed to the

difference in atomic radius between titanium and oxygen. On the other hand, the atomic percentages of both elements (Ti and O) are comparable (46% and 54%, respectively). These results show that the synthesized nanopowder certainly contains non-stoichiometric TiO_2 compound. However, the intended uses of the synthesized nanopowders do not critically need for stoichiometric compound.

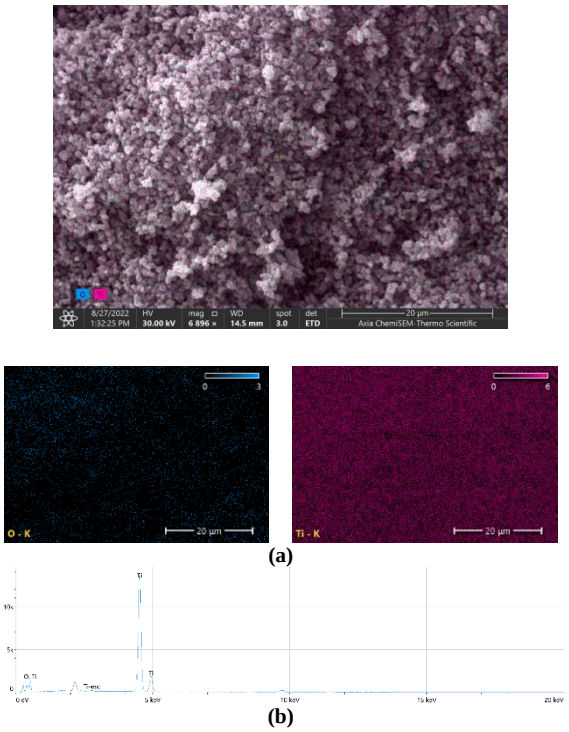

(a)

(b)

Element	Atomic %	Atomic % Error	Weight %	Weight % Error
O	54.0	2.90	26.8	1.55
Ti	46.0	0.21	73.1	0.35

Fig. (3) EDX result of synthesized TiO_2 nanopowder (a) color map distribution, (b) EDX spectrum and elemental analysis table

Figure (4) shows the FTIR spectrum of the TiO_2 nanopowder synthesized in this work. There are three distinct peaks centered at 409, 447 and 667 cm^{-1} belonging to the vibrations of the TiO_2 molecules in the TiO_2 lattice; bending, asymmetric and symmetric modes, respectively [20]. As well, two bands at 1620 and 3450 cm^{-1} are clearly seen and they are attributed to the vibration modes of O-H bond. The two possible sources for the OH molecules are (1) the aqueous solution included in the synthesis route, and (2) adsorption of water molecules from the environment when the synthesized sample is exposed to the atmosphere [21,22].

Since the antibacterial and antifungal activity of TiO_2 nanopowder depends on its absorption characteristics, then the assessment of the synthesized nanopowder can be done by recording the absorption spectrum of this nanopowder. However, the synthesized nanopowder should be hosted in a less-dense medium to record its absorption spectrum after been referenced to the absorption spectrum of the hosting medium. Figure (5) shows the UV-visible spectrum of the synthesized TiO_2 nanopowder in the spectral range of 300-800 nm.

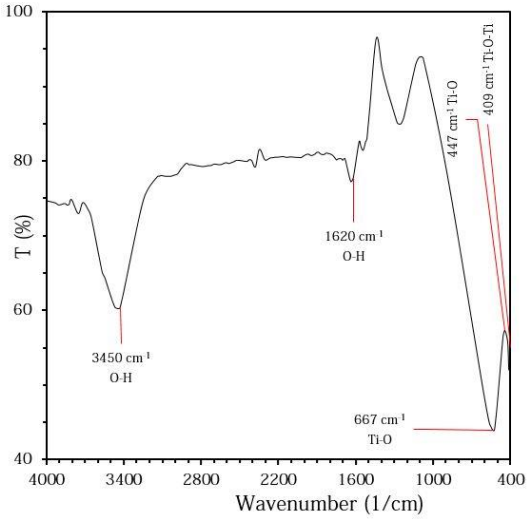

Fig. (4) FTIR spectrum of synthesized TiO_2 nanopowder

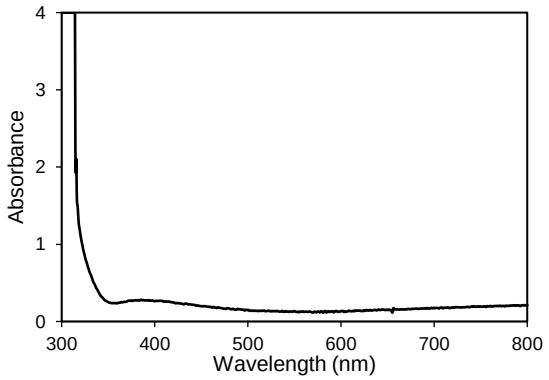

Fig. (4) UV-visible spectrum of synthesized TiO_2 nanopowder

It is clear that the sample exhibits high absorption in the UV region (<400nm) and very low absorption in the visible and near-infrared (NIR) regions. Such behavior is a characteristic of TiO_2 as its photocatalytic activity is induced by the absorption of UV radiation. Therefore, the synthesized nanopowder can be successfully and safely used for antibacterial and antifungal purposes due to the synergetic effect exhibited by the TiO_2 nanostructures containing both anatase and rutile phases [23,24].

4. Conclusion

In concluding remarks, mixed-phase TiO_2 nanopowder was synthesized by solvothermal method using banana peels and titanium isopropoxide as titanium precursor. The structural characteristics have confirmed that the synthesized nanopowder is polycrystalline and containing both anatase and rutile phases. A minimum nanoparticle size of 25.41 nm was observed. Also, the synthesized nanopowder showed reasonable structural purity as no other

 © ALL RIGHTS RESERVED

elements other than Ti and O were detected in the final sample. Spectroscopic characteristics of the synthesized nanopowder confirmed that it can be successfully used for practical applications based on the photocatalytic activity of TiO_2 nanomaterial. The proposed method can be described as low-cost, reliable and simple enough to provide the practical applications requiring mass quantities of TiO_2 nanopowders.

References

[1] P. Nyamukamba et al., "Synthetic Methods for Titanium Dioxide Nanoparticles: A Review", Ch. 8, in **"Titanium Dioxide - Material for a Sustainable Environment"**, edited by D. Yang, IntechOpen (2018).

[2] S. Chaiyakun et al., "Growth and characterization of nanostructured anatase phase TiO_2 thin films prepared by DC reactive unbalanced magnetron sputtering", *Appl. Phys. A*, 95(2) (2009) 579-587.

[3] X. Chen and S.S. Mao, "Titanium Dioxide Nanomaterials: Synthesis, Properties, Modifications, and Applications", *Chem. Rev.*, 107(7) (2007) 2891-2959.

[4] K. Zakrzewska and M. Radecka, "TiO_2-Based Nanomaterials for Gas Sensing - Influence of Anatase and Rutile Contributions", *Nanoscale Res. Lett.*, 12 (2017) 89-96.

[5] H.A. Alhadrami et al., "Antibacterial Applications of Anatase TiO_2 Nanoparticle", *Am. J. Nanomater.*, 5(1) (2017) 31-42.

[6] J.O. Carneiro et al., **"Self-cleaning smart nanocoatings, Nanocoatings and Ultra-Thin Films: Technologies and Applications"**, Woodhead Publishing Series in Metals and Surface Engineering, 2011, Pages 397-413.

[7] E.A. Al-Oubidy and F.J. Al-Maliki, "Photocatalytic activity of anatase titanium dioxide nanostructures prepared by reactive magnetron sputtering technique", *Opt. Quantum Electron.*, 51(1-2) (2019) 23.

[8] M. Aravind, M. Amalanathan and M. Sony Michael Mary, "Synthesis of TiO_2 nanoparticles by chemical and green synthesis methods and their multifaceted properties", *SpringerNature Appl. Sci.*, 3 (2021) 409.

[9] M. Sundrarajan and S. Gowri, "Green synthesis of titanium dioxide nanoparticles by nyctanthes arbor-tristis leaves extract", *Chalcog. Lett.*, 8(8) (2011) 447-451.

[10] X. Yue et al., "High surface area, high catalytic activity titanium dioxide aerogels prepared by solvothermal crystallization", *J. Mater. Sci. Technol.*, 47 (2020) 223-230.

[11] J. Biener et al., "Surface Chemistry in Nanoscale Materials", *Materials*, 2 (2009) 2404-2428.

[12] F.J. Al-Maliki, O.A. Hammadi and E.A. Al-Oubidy, "Optimization of Rutile/Anatase Ratio in Titanium Dioxide Nanostructures prepared by DC Magnetron Sputtering Technique", *Iraqi J. Sci.*, 60(special issue) (2019) 91-98.

[13] V.H. Castrejón-Sánchez, E. Camps and M. Camacho-López, "Quantification of phase content in TiO_2 thin films by Raman spectroscopy", *Superficies y Vacío*, 27(3) (2014) 88-92.

[14] C. Byrne et al., "New approach of modifying the anatase to rutile transition temperature in TiO_2 photocatalysts", *RSC Adv.*, 97(6) (2016) 95232-95238.

[15] I. Karabay et al., "Structural and Optical Characterization of TiO_2 Thin Films Prepared by Sol–Gel Process", *Acta Physica Polonica A*, 121(1) (2012) 265-267.

[16] C.S. Kim et al., "Solvothermal synthesis of nanocrystalline TiO_2 in toluene with surfactant", *J. Cryst. Growth*, 257 (2003) 309-315.

[17] JCPDS card no. 3-0380 (TiO_2), **"Standard X-ray Diffraction Powder Patterns"**, US Department of Commerce, National Bureau of Standards, Vol. 25, Sec. 3, p. 57.

[18] A. Monsi, M.R. Foroughi and M.R. Monshi, "Modified Scherrer Equation to Estimate More Accurately Nano-Crystallite Size Using XRD", *World J. Nano Sci. Eng.*, 2 (2012) 154-160.

[19] F.J. Al-Maliki and E.A. Al-Oubidy, "Effect of gas mixing ratio on structural characteristics of titanium dioxide nanostructures synthesized by DC reactive magnetron sputtering", *Physica B: Cond. Matter*, 555 (2019) 18-20

[20] N.N. Greenwood and E.J.F. Ross, **"Index of Vibrational Spectra of Inorganic and Organometallic Compounds"**, vol. III, The Butterworth Group (London, 1966) p. 1078.

[21] Y. Bouachiba et al., "Structural and optical properties of TiO_2 thin films grown by sol-gel dip coating process", *Mater. Sci. Poland*, 32(1) (2014) 1-6.

[22] F.J. Al-Maliki and N.H. Al-Lamey, "Synthesis of Tb-Doped Titanium Dioxide Nanostructures by Sol-Gel Method for Environmental Photocatalysis Applications" *J. Sol-Gel Sci. Technol.*, 81(1) (2017) 276-283.

[23] F. Amano et al., "Photocatalytic activity of octahedral single-crystalline mesoparticles of anatase titanium(IV) oxide", *Chem. Commun.*, 17 (2009) 2311-2313.

[24] A. Zachariah et al., "Synergistic Effect in Photocatalysis As Observed for Mixed-Phase Nanocrystalline Titania Processed via Sol-Gel Solvent Mixing and Calcination", *J. Phys. Chem. C*, 112(30) (2008) 11345-11356.

IRAQI JOURNAL OF APPLIED PHYSICS
Vol. 18, No. 4, October-December 2022, pp. 31-36

Structural and Optical Characteristics of Co_3O_4 Nanostructures Prepared by DC Reactive Magnetron Sputtering

Noor Alhuda H. Hashim
Firas J. Kadhim

Department of Physics, College of Science, University of Baghdad, Baghdad, IRAQ

Cobalt oxide thin films were prepared by dc reactive magnetron sputtering system using different gas mixing ratios of argon and oxygen. The influence of gas mixing ratio on the structure of cobalt oxide thin film was studied by x-ray diffraction (XRD) patterns, which confirm the crystalline nature of the prepared samples. A well-defined diffraction peak at about 37° (311) was observed, which indicates that the spinel structure (Co_3O_4) of cobalt oxide was obtained. The particle size of the prepared Co_3O_4 was determined by field-emission scanning electron microscopy (FE-SEM) and the elemental composition of this oxide was evaluated by energy-dispersive x-ray dispersive (EDX) spectroscopy. The energy band gap was determined in the range 2.01-2.06 eV. Due to the homogeneous optical and structural characteristics of the prepared cobalt oxide thin films, they can be used as ion-storage layer in electrochromic or photoelectrochromic device.

Keywords: Cobalt oxide; Reactive sputtering; Magnetron sputtering; Nanostructures
Received: 30 September 2022; **Revised:** 26 October 2022; **Accepted:** 2 November 2022

1. Introduction

Cobalt oxide is one of the most important transition metal oxide, p-type antiferromagnetic semiconductors. Cobalt forms two stable oxides: cubic-type structure (CoO) with direct band gap between 2.2-2.8 eV [1,2], and spinel-type structure (Co_3O_4) with direct band gap between 1.48-2.19 eV [3]. Cobalt oxide nanostructures have a wide range of applications due to their shape-dependent activities and unique size, optical, magnetic, electronic, chemical, electrochemical, mechanical properties [4,5]. There are several deposition techniques to prepare oxide thin films such as sputtering, chemical vapor deposition, spray pyrolysis, electrophoretic deposition (EPD), pulsed laser deposition (PLD), sol-gel process, etc. [6,7]. The reactive sputtering is a frequently employed technique for deposition of thin films, in combination with reactive gases like oxygen and nitrogen, for the deposition of oxide and nitride films [8-15]. This technique has been considered to be promising for the preparation of high quality, high purity, and homogeneity and it is also much better to produce layers of compound materials and alloys in order to control the formation and structural phase of the deposited nanostructured films [16-22]. The preparation and characterization of cobalt oxides have been extensively studied due to attractive applications in batteries, catalysis, corrosion protective coatings, solar cells, magnetic nanostructures, magnetic storage systems, and electrochromic (EC) device. Co_3O_4 has been reported to be a good anodic coloration material for the EC application [5,23].

The dc reactive magnetron sputtering technique will be employed to prepare nanostructured cobalt oxide thin films and study their structural characteristics in order to use these films as a counter electrode (ion-storage layer).

2. Experimental Part

A homemade dc reactive magnetron sputtering system was used to deposit cobalt oxide thin films on glass substrates. This system works under vacuum which ensures high structural purity of the prepared films. A cobalt sheet (diameter of 6 cm, thickness of 1 mm, purity of 99.99%) supplied by Stanford Advanced Materials was mounted on the cathode as a target and the glass substrate was placed on the anode [24,25]. The substrates were cleaned by ethanol to remove any residuals on their surfaces and then rinsed in distilled water to remove the ethanol. The inter-electrode distance was varied from 4 to 9 cm in order to determine the optimum distance for producing high quality samples (i.e., highly uniform film thickness) and was fixed at 4 cm. Several samples were prepared using different gas mixing ratios of argon and oxygen ($Ar:O_2$) (60:40, 70:30, 80:20 and 90:10) to produce the Co_3O_4 structural phase and study the effect of changing this ratio on the particle size. Plasma was produced by electrical discharge of argon gas at pressure of 7.2×10^{-2} mbar, the lowest electrical power was 24 W, with applied voltage of 1.6 kV and

 © ALL RIGHTS RESERVED

discharge current of 15 mA. Figure (1a) shows the sample of cobalt oxide thin film deposited on silica substrate after deposition time of 1 hour.

Nanopowders were extracted from deposited thin films using the conjunctional freezing-assisted ultrasonic extraction technique, which is quick, low-cost, reliable, and extremely clean [26-28]. Figure (1b) shows the extracted powder.

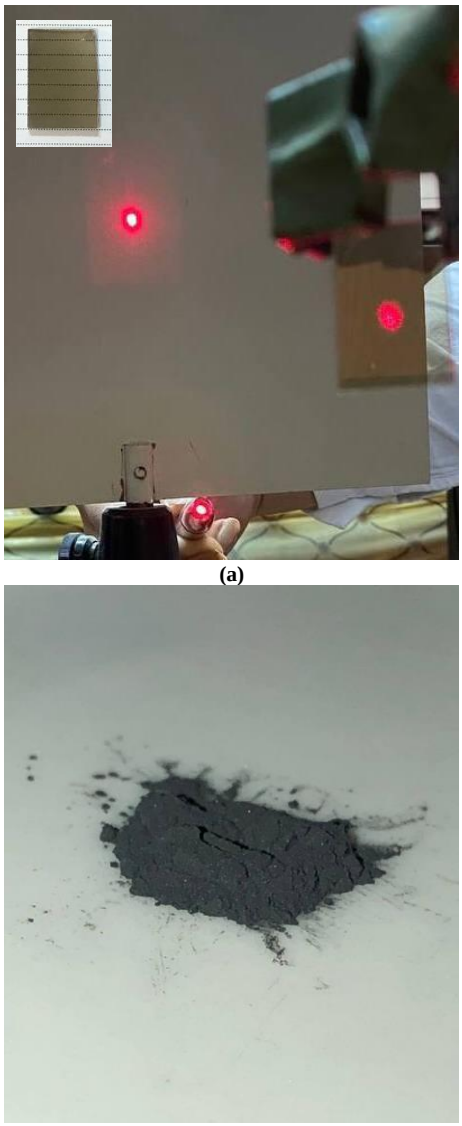

(a) **(b)**

Fig. (1) (a) Cobalt oxide thin film prepared in this work, and (b) the extracted nanopowder from thin film samples

3. Results and Discussion

The crystal structure of the powders extracted from cobalt oxide thin films was investigated by an X-ray Shimadzu Diffractometer using Cu-Kα source (1.54Å). The XRD shows several peaks which are attributed to typical spinel-type cobalt oxide. All recorded XRD patterns of cobalt oxide nanopowders prepared with different gas (Ar:O_2) mixing ratios indicate that the crystalline structure of the deposited films constitutes a single phase of Co_3O_4 with a spinel-type structure. The XRD patterns in Fig. (2) show a major peak at about 37° corresponding to crystal plane of (311). This peak has the highest intensity, indicating the oriented growth of the sample in the (311) direction. We have observed peaks at 31.5°, 37.1°, 38.7°, 45.0°, 55.9°, 59.6°, and 65.4° corresponding to (220), (311), (222), (400), (422), (511) and (440) planes, which indicate the formation of pure Co_3O_4 [29], and no other peaks are observed from any impurity due to the use of sputtering technique in this work. The intensities of peaks are affected by particle size and their full-width-at-half maximum (FWHM) is inversely proportional to the crystallite size, as FWHM increases with decreasing crystallite size, the FWHM of prepared samples are 0.4949, 0.4223, 0.3397 and 0.2397 for mixing ratios of (60:40), (70:30), (80:20) and (90:10), respectively. The crystallite size is proportional to the intensity of diffraction peaks, then the intensity of diffraction peak for the sample prepared using (60:40) mixing ratio is lower than other morphologies of Co_3O_4 prepared using other (Ar:O_2) gas mixing ratios, suggesting that spinel Co_3O_4 prepared using (60:40) mixing ratio may has lower crystallinity and smaller crystallite size [30].

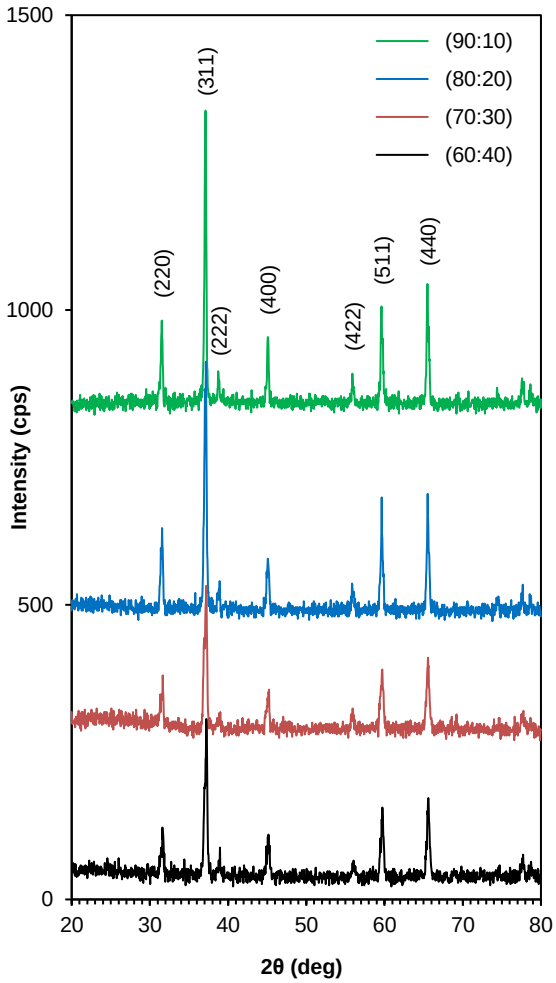

Fig. (2) XRD patterns of Co_3O_4 samples prepared using different gas mixing ratios

According to Scherrer's formula, the average crystallite size (D) of the Co_3O_4 sample is estimated from the XRD pattern as [31]:

$$D = \frac{K\lambda}{\beta cos\theta} \quad (1)$$

where λ is the x-ray source wavelength (1.54Å), β is the FWHM, K is a dimensionless shape factor with value of 0.9, and θ is the diffraction angle of incident radiation

The (311) diffraction peak of Co_3O_4 sample prepared using (60:40) mixing ratio shows peak width larger than others, indicating that the crystalline size of such Co_3O_4 sample is smaller than the Co_3O_4 samples prepared using other gas mixing ratios. The calculated crystallite size is found to be 16.00, 18.76, 23.32 and 33.05 nm for samples prepared using mixing ratios of (60:40), (70:30), (80:20) and (90:10), respectively. In dc sputtering deposition, the power has an important role to control the structure of the prepared cobalt oxide sample [32], and as mentioned in the experimental part, we have used low deposition power (14W). This structure of cobalt oxide is promising anodically coloring electrochromic material, thus, it can be used as a counter electrode in the electrochromic device.

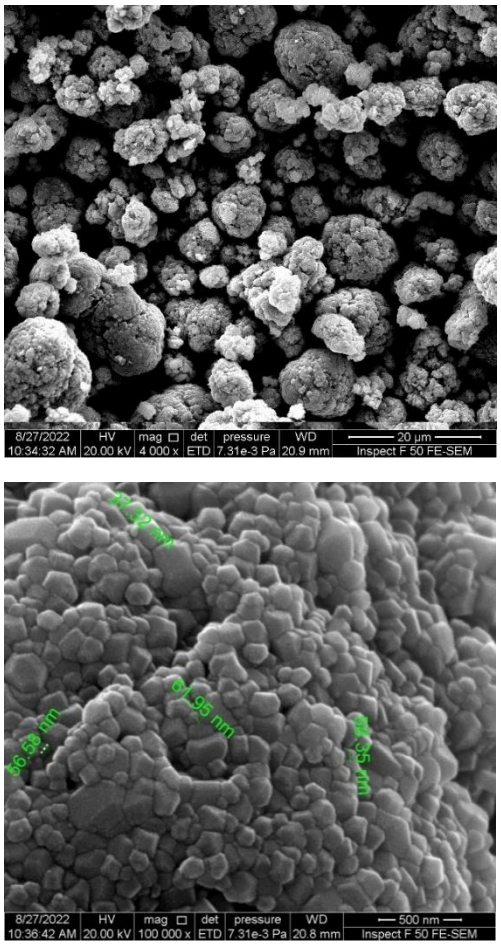

Fig. (3) FE-SEM images of Co_3O_4 nanostructures prepared using gas mixing ratio of (60:40)

The nanoparticle size of Co_3O_4 samples was studied by field-emission scanning electron microscopy (FE-SEM), as shown in Fig. (3), with different magnifications. The image with scale of 500 nm shows the spherical shape of nanoparticles, with minimum particle size of 37.32 nm, and the aggregated particles indicating a good connectivity between these nanoparticles.

The nanoparticles can form complex assemblies referred as aggregates, which typically consist of particles in the nanoscale (5-50) nm and are held together by weaker forces arising from van der Waals and electrostatics effects. Ambient humidity plays an important role in determining the fundamental mechanical response and dynamics of the assemblies [33]. The FE-SEM image indicates that the prepared nanoparticles are uniformly distributed. This type of morphology is beneficial to use cobalt oxide as a counter electrode (ion storage layer) for EC device and supercapacitor application [34].

The elemental composition of the prepared Co_3O_4 nanostructures was evaluated by the EDX analysis. According to Fig. (4), the major peaks are for the Co and O forming the cobalt oxide sample, and the minor peak attributed to the C, which results from handling the sample inside the instrument. The elemental composition of the cobalt oxide nanostructures shows 72.3% of cobalt, 19.9% of oxygen corresponding to the structural phase of Co_3O_4 and 7.8% of carbon. Using sputtering technique, the formation of nanostructures with required composition can be controlled by controlling the gas mixing ratio. Also, many metal oxides can be prepared by sputtering technique with good control of their compositions.

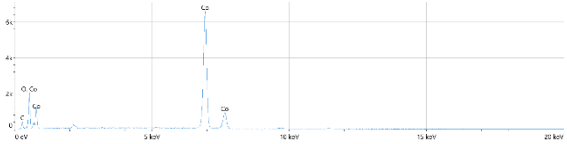

Fig. (4) EDX spectrum of cobalt oxide (Co_3O_4) prepared using gas mixing ratio of (60:40)

Figure (5) shows the FTIR spectrum of the sample prepared at inter-electrode distance of 4 cm, deposition time of 1 hour, and gas mixing ratio of (60:40). This spectrum was recorded in the range from 400 to 4000 cm^{-1}. Two strong peaks were observed; the first at 572.82 cm^{-1} was assigned to Co-O stretching vibration mode, in which Co^{+3} is octahedrally coordinated, and the second peak at 663.47 cm^{-1} was assigned to bridging vibration, in which Co^{+2} is tetrahedrally coordinated [35]. This further confirms the formation of Co_3O_4. The peaks at 1571.88 and 3436.91 cm^{-1} are ascribed to the OH stretching and banding modes of water adsorbed by the sample. The peaks at 2408.93 and 1423.37 cm^{-1} are characteristic of asymmetric vibrations of CO_2 and CO^{-2} which were also adsorbed from the air [36].

 © ALL RIGHTS RESERVED

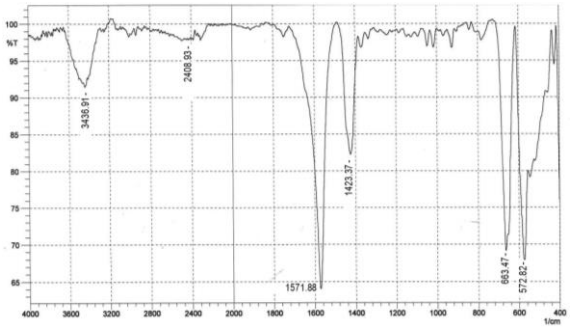

Fig. (5) FTIR spectrum of Co_3O_4 sample prepared using gas mixing ratio of (60:40)

Figure (6) shows the absorption spectra of the prepared Co_3O_4 thin film samples recorded by a UV-visible spectrophotometer within the spectral range of 400-700 nm while the measurement was carried out within 200-800 nm. The prepared thin films did not show spectral activity at wavelengths shorter than 400 nm and longer than 700 nm. The increase of absorbance is proportional to the increase of oxygen content in the gas mixture. This is attributed to the formation of more Co_3O_4 nanoparticles. Also, due to increasing oxygen content in the gas mixture, the measurements show very slight blue shift in the absorption edge towards shorter wavelengths [37].

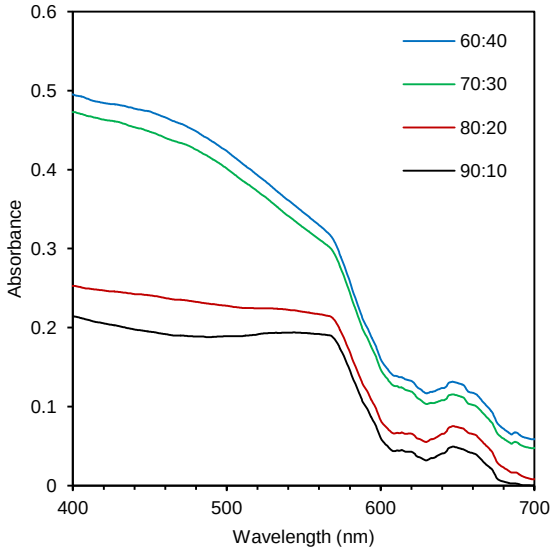

Fig. (6) Absorption spectra of cobalt oxide thin films prepared using different gas mixing ratios

The relationship between the photon energy and absorption coefficient can be used to determine the energy gap applying the Tauc's equation [38]:

$$(\alpha h\nu) = A(h\nu - E_g)^n \quad (2)$$

where A is a constant, E_g is the band gap energy and n is a constant, taking values of 1/2 or 2 for indirect and direct allowed transitions, respectively

Figure (7) shows the determination of energy band gap for cobalt oxide thin films prepared using gas mixing ratios of (90:10), (80:20), (70:30) and (60:40) to be 2.01, 2.03, 2.05 and 2.06 eV, respectively. This result is in agreement with the range of 1.48-2.19 eV for the Co_3O_4 [39].

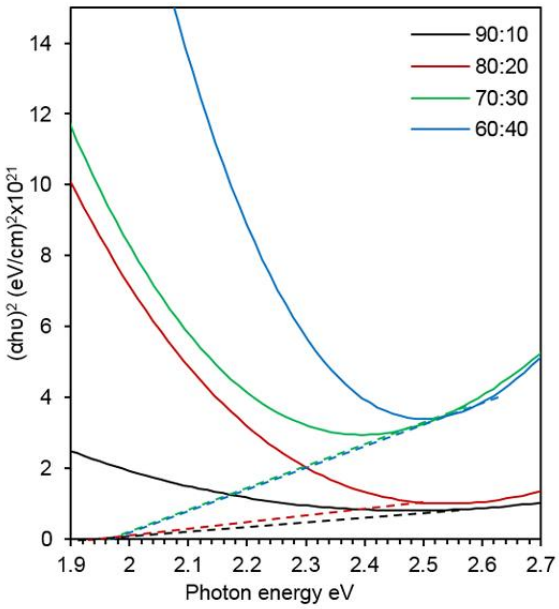

Fig. (7) Determination of energy band bap for cobalt oxide samples prepared using different gas mixing ratios

4. Conclusions

In conclusions, high quality and high homogeneity cobalt oxide (Co_3O_4) nanostructures were successfully prepared using dc reactive magnetron sputtering technique. As a sputtering parameter, working/reactive (Ar/O_2) gas mixing ratio plays a key role for controlling the structural characteristics of such oxide. This structure of cobalt oxide (Co_3O_4) can be used as ion-storage layer in electrochromic or photoelectrochromic applications, due to its structural and optical properties, such as uniform distribution of nanoparticles, particle size, absorbance and high transmittance.

References

[1] I.P. Koziarskyi et al., "Optical Properties of Cobalt Oxide Thin Films", IEEE Int. Conf. on Nanomaterials: Applications & Properties, (NAP-2020), Sumy, Ukraine, 9-13 Nov. 2020

[2] O.A. Hammadi and N.E. Naji, "Fabrication and Characterization of Polycrystalline Nickel Cobaltite Nanostructures Prepared by Plasma Sputtering as Gas Sensor", Phot. Sen., 8(1) (2018) 43-47.

[3] V. Patil et al., "Synthesis and Characterization of Co_3O_4 Thin Film", Sci. Res., 2(1) (2012) 1-7.

[4] H. Heli and H. Yadegari, "Nanoflakes of the cobaltous oxide, CoO: Synthesis and characterization", Electrochimica Acta, 55 (2010) 2139-2148.

[5] A.E. Kaloyeros et al., "Review–cobalt thin films: trends in processing technologies and emerging applications", ECS J. Solid State Sci. Technol., 8 (2019) 119.

[6] R. Drasovean, S. Condurache-Bota and N. Tigau, "Structural and Electrical Characterization of Cobalt Oxide Semiconductors", J. Sci. Arts, 13(2) (2010) 379-384.
[7] R. Hippler et al., "Deposition of cobalt oxide films by reactive pulsed magnetron sputtering", Surf. Coat. Technol., 405 (2021) 126590.
[8] M.K. Khalaf, F.J. Kadhim and O.A. Hammadi, "Effect of Adding Nitrogen to the Gas Mixture on Plasma Characteristics of a Closed-Field Unbalanced DC Magnetron Sputtering System", Iraqi J. Appl. Phys., 10(1) (2014) 27-31.
[9] O.A. Hammadi, M.K. Khalaf and F.J. Kadhim, "Fabrication of UV Photodetector from Nickel Oxide Nanoparticles Deposited on Silicon Substrate by Closed-Field Unbalanced Dual Magnetron Sputtering Techniques", Opt. Quantum Electron., 47(12) (2015) 3805-3813.
[10] M.A. Hameed and Z.M. Jabbar, "Preparation and Characterization of Silicon Dioxide Nanostructures by DC Reactive Closed-Field Unbalanced Magnetron Sputtering", Iraqi J. Appl. Phys., 12(4) (2016) 13-18.
[11] O.A. Hammadi, M.K. Khalaf and F.J. Kadhim, "Fabrication and Characterization of UV Photodetectors Based on Silicon Nitride Nanostructures Prepared by Magnetron Sputtering", Proc. IMechE, Part N, J. Nanomater. Nanoeng. Nanosys., 230(1) (2016) 32-36.
[12] O.A. Hammadi, M.K. Khalaf and F.J. Kadhim, "Silicon Nitride Nanostructures Prepared by Reactive Sputtering Using Closed-Field Unbalanced Dual Magnetrons", Proc. IMechE, Part L, J. Mater.: Design & Appl., 231(5) (2017) 479-487.
[13] R.H. Turki and M.A. Hameed, "Spectral and Electrical Characteristics of Nanostructured NiO/TiO_2 Heterojunction Fabricated by DC Reactive Magnetron Sputtering", Iraqi J. Appl. Phys., 16(3) (2020) 39-42.
[14] N.H. Mutesher and F.J. Kadhim, "Comparative Study of Structural and Optical Properties of Silicon Dioxide Nanoparticles Prepared by DC Reactive Sputtering and Sol-Gel Route", Iraqi J. Appl. Phys., 17(1) (2021) 17-20.
[15] F.J. Kadhim, O.A. Hammadi and A.A. Anber, "Spectroscopic Study of Chromium-Doped Silicon Nitride Nanostructures Prepared by DC Reactive Magnetron Sputtering", Iraqi J. Appl. Phys., 17(2) (2021) 9-12.
[16] R. Hippler et al., "Characterization of a magnetron plasma for deposition of titanium oxide and titanium nitride films", Contrib. Plasma Phys., 45 (2005) 348-357.
[17] F.J. Al-Maliki and M.A. Al-Rubaiy, "Synthesis and study the concentration effect on the photocatalytic activity of titania nanoparticles as anti-bacteria using reactive magnetron sputtering technique", Opt. Quant. Electron., 54 (2022) 377.
[18] F.J. Kadhim and A.A. Anber, "Highly-Pure Nanostructured Silicon Nitride Films Prepared by Reactive DC Magnetron Sputtering", J. Indust. Eng. Sci., 25(5) (2016) 91-94.
[19] A.A. Anber and F.J. Kadhim, "Preparation of Nanostructured Si_xN_{1-x} Thin Films by DC Reactive Magnetron Sputtering for Tribology Applications", Silicon, 10 (2018) 821-824.
[20] M.A. Hameed and Z.M. Jabbar, "Optimization of Preparation Conditions to Control Structural Characteristics of Silicon Dioxide Nanostructures Prepared by Magnetron Plasma Sputtering", Silicon, 10(4) (2018) 1411-1418.
[21] B.K. Nasser and M.A. Hameed, "Structural Characteristics of Silicon Nitride Nanostructures Synthesized by DC Reactive Magnetron Sputtering", Iraqi J. Appl. Phys., 15(4) (2019) 33-36.
[22] M.A. Hameed, S.H. Faisal, R.H. Turki, "Characterization of Multilayer Highly-Pure Metal Oxide Structures Prepared by DC Reactive Magnetron Sputtering Technique", Iraqi J. Appl. Phys., 16(4) (2020) 25-30
[23] L.D. Kadam, S.H. Pawar and P.S. Patil, "Studies on ionic intercalation properties of cobalt oxide thin films prepared by spray pyrolysis technique", Mater. Chem. Phys., 68 (2001) 280-282.
[24] O.A. Hammadi et al., "Operation Characteristics of a Closed-Field Unbalanced Dual-Magnetrons Plasma Sputtering System", Bulg. J. Phys., 41(1) (2014) 24-33.
[25] E.A. Al-Oubidy and F.J. Kadhim, "Effect of Gas Mixing Ratio on Energy Band Gap of Mixed-Phase Titanium Dioxide Nanostructures Prepared by Reactive Magnetron Sputtering Technique", Iraqi J. Appl. Phys., 14(4) (2018) 19-23.
[26] O.A. Hammadi, "Production of nanopowders from physical vapor deposited films on nonmetallic substrates by conjunctional freezing-assisted ultrasonic extraction method", Proc. IMech. Eng. Part N: J. Nanomater. Nanoeng. Nanosyst, 232(4) (2018) 135-140.
[27] O.A. Hammadi, "Conjunctional Freezing-Assisted Ultrasonic Extraction of Silicon Dioxide Nanopowders from Thin Films Prepared by Physical Vapor Deposition Technique", Iraqi J. Appl. Phys., 15(4) (2019) 23-28.
[28] O.A. Hammadi, "Effects of Extraction Parameters on Particle Size of Titanium Dioxide Nanopowders Prepared by Physical Vapor Deposition Technique", Plasmonics, 15(6) (2020) 1747-1754.
[29] H.E. Swnason et al., **"Standard X-Ray Diffraction Powder Patterns"**, International Center for Diffraction Data (ICDD) (Washington DC, 1971), NBS monograph 25, Sec. 9, p. 29

 © ALL RIGHTS RESERVED

[30] X. Zhu et al., "Co_3O_4 nanoparticles with different morphologies for catalytic removal of ethyl acetate", Catal. Comm., 156 (2021) 106320.
[31] C. Suryanarayana, **"Mechanical Alloying and Milling"**, Marcel Dekker (NY, 2004), Ch. 7, p. 111.
[32] N. Francelosi et al., "Role of the reactive sputtering deposition power in the phase control of cobalt oxide films", Am. Vac. Soc., 36 (2018) 061512.
[33] S.C. Endres, L.C. Ciacch and L. Madler, "A review of contact force models between nanoparticles in agglomerates, aggregates and films", J. Aerosol Sci., 153 (2021) 105719.
[34] R. Lakra et al., "Synthesis and characterization of cobalt oxide (Co_3O_4) nanoparticles", Mater. Today: Proc., 2 September 2020.
[35] K. Maaz, **"Cobalt"**, InTech Open (Croatia, 2017), Ch. 4, p. 56.
[36] A.N. Naveen and S. Selladurai, "Investigation on physiochemical properties of Mn substituted spinel cobalt oxide for supercapacitor applications", Electrochimica Acta, 125 (2014) 404-414.
[37] S. Baset et al., "Size measurement of metal and semiconductor nanoparticles via UV-vis absorption spectra", Dig. J. Nanomater. Biostruct., 6(1) (2011) 1-8.
[38] R. Saravanan, **"Novel Ceramic Materials"**, Materials Research Forum LLC (Millersville PA, 2016), Vol. 2, Ch. 4, p. 49.
[39] M. Kumar Patel et al., "Reactive sputtering growth of Co_3O_4 thin films for all metal oxide device: a semitransparent and self-powered ultraviolet photodetector", Mater. Sci. Semicond. Process., 74 (2018) 74-79.

Iraqi Journal of Applied Physics

P. O. Box 55259, Baghdad 12001, IRAQ
www.iraqiphysicsjournal.com
Email: info@iraqiphysicsjournal.com
Email: editor_ijap@yahoo.co.uk
Email: irq_appl_phys@yahoo.com
Email: ijap.editor@gmail.com

Subject Index 2005-2022

Alternative & Renewable Energy
IJAP-AARE

- General Characteristics of High Energetic Proton Events Observed with SOHO/ERNE During Solar Cycle 23, 10(4), 3
- Nuclear Green Energy, 10(1), 3
- Characterization of Laser-Ablated Nanostructured Al_2O_3/p-Solar Cells, 11(1), 29

Applied & Nonlinear Optics
IJAP-AANO

- Analytical Study on Effect of Lateral Shear Interferogram on Path Difference in Coherent Optical Systems, 18(2), 11
- Computer Aided Design of a Magnetic Lens Using a Combined Dynamic Programming and Artificial Intelligence Technique, 10(1), 33
- Control of Nonlinear Dynamics in Semiconductor Laser with Optoelectronic Feedback, 15(1), 3
- Curvelet-Based Optical Flow Estimation Algorithm Based on Central Derivatives, 6(2), 13
- Design of a Multi-Electrode Immersion Lens for Ion-Optical Systems, 2(1,2), 27
- Design of All-Reflecting Aplanatic Objective, 9(3), 19
- Development of an Inverted Optical Tweezers with Full Motional Control, 7(2), 19
- Investigations of Linear and Nonlinear Optical Properties of Transparent ZnO Thin Films Grown by Sol-Gel Method, 6(3), 29
- Key Mechanisms of the Nonlinear Amplification: Physics and Applications, 1(2), 3
- Microscopic Imaging of Red Cell Aggregation with Photoacoustic Technique, 18(4), 3
- Microstructual Features and Properties of High-Hardness and Heat-Resistant Dispersion Strengthened Copper by Reaction Milling, 8(4), 3
- New Method for Calculating Cumulative Line Energy Using Pupil Function Technique, 2(1,2), 7
- Numerical Analysis of Temperature Dependencies of Optical Elasticity Coefficient on Lens Induced in Solid-State Laser Crystal, 14(2), 35
- Some Optical Properties of an Electrostatic Immersion Lens Using the Charge Density Method, 1(4), 21
- Tapering and Metallizing Optical Fibers by Immersion in Buffered Aqueous Solution with Different Molar Ratios, 18(2), 33
- Temperature-Dependent Birefringence Properties of $Be_3Al_2Si_6O_{18}$ Crystal, L2(1), 12
- Thermogravimetric Properties of Porcelain Supported by Addition of Beryllium Oxide, 17(3), 27

Applied Mechanics & Thermodynamics
IJAP-AMAT

- Analytical and Experimental Study on Bound and Free Surface Waves in Wind-Wave Tank System, 8(1), 11
- Analytical Calculation of Heat Conduction in Two-Phase Heterogeneous Materials, 7(4), 11
- Characterization of D.C. Sputtering System, L1(1), 3
- Employing Inner Triplet Upgrade in Cold Mass Cooling Design for Large Hadron Collider, L2(1), 19
- Ferrohydrodynamic Instability of a Couple Stress Magnetic Fluid Layer Under the Influence of Time-Dependent Sinusoidal Magnetic Field, 18(4), 15
- HAZ Extent Analysis in Fiber-Reinforced Plastic Grooving by Laser, 1(1), 3
- Investigation of Bound and Free Surface Waves in Microwave and Acoustic Wind-Wave Tank Systems, 14(2), 11
- Optimization of Composition, Structure and Characteristics of Metal in Arc Deposition, 5(2), 37
- Marangoni Convection Effect on the Melting of GaSb/InSb/GaSb Sandwich Structured Sample, 4(2), 35
- Modeling of the Preheating Effect on Keyhole Laser Welding Efficiency, L1(1), 10
- Performance of Thermally Regenerative Electrochemical Cycles System, 18(2), 3
- Structural, Electronic and Thermal Properties of TiC Compound in Sodium Chloride Structure, 11(1), 9
- Torque and Magnetic Flux Analysis Using an Advanced Dynamic Dynamometer Test Bed for Electromechanical Motors, 5(1), 13
- Using Longitudinal Surface Acoustic Waves for Non-Destructive Testing of Inner Surfaces, L1(2), 9

Digital & Optical Communications
IJAP-DAOC

- A Balanced Backoff Algorithm for IEEE802.11 Wireless Network, 8(1), 27
- A CPW-Fed Printed Monopole Ultra-Wideband Antenna with E-Shaped Notched Band Slot, 6(4), 17
- A New Fractal Microstrip Bandpass Filter Design Based on Dual-Mode Square Ring Resonator for Wireless Communication Systems, 5(1), 7
- A Novel Secure Digital Watermark Generation from Public Share by Using Visual Cryptography and MAC Techniques, 10(3), 3

All Rights Reserved ISSN (printed) 1813-2065, (online) 2309-1673 Printed in IRAQ

Electronic Materials & Devices

IJAP-EMAD

© 2022 Iraqi Society for Alternative and Renewable Energy Sources and Techniques (I.S.A.R.E.S.T.)

Environment Science & Technology
IJAP-ENST

- Determination of Uranium and Thorium levels and Measurement of Annual Effective Dose levels in Some Canned Foods, 18(3), 31
- Using Banana Peels for Green Synthesis of Mixed-Phase Titanium Dioxide Nanopowders, 18(4), 21

Laser Physics & Applications
IJAP-LPAA

- (3-5)μm and (8-12)μm Wavelengths Ultra-Short Tunable Laser Pulses Using Optical Parametric Oscillation Technique, 4(4), 37
- A Line Tuned TM_{00} Mode CW CO_2 Laser, 1(1), 8
- Accurate Relative Frequency Cancellation Between Two Independent Lasers, 2(3,4), 3
- Characterization of Diode Laser-Pumped Nd:YVO_4 Disk Laser, 4(2), 31
- Characterization of Quantum Well Diode Pumped Nd:YVO_4 Using V-Shape Technique, L1(1), 31
- Continuous-Wave Broadly Tunable Cr^{2+}:ZnSe Laser, 2(3,4), 6
- Design and Simulation of DPSS Laser with SHG for Material Processing, L2(1), 3
- Design and Simulation of Q-Switching and Mode-locking Nonlinear Mirror for Frequency-Doubled DPSS Nd:YAG Laser Output, 7(4), 23
- Design, Construction and Operation of a Multi-Stage Large-Bore CO_2 Laser, 1(1), 25
- Development of UV Raman LIDAR System to Measure Temperature and Water Vapour Profiles in Troposphere Layer, 14(2), 19
- Effect of Active Medium Temperature on the Output Characteristics of Pulsed Free-Running R6G and RB Dye Laser, 1(1), 30
- Effect of Self-Absorption on the Output Power of CW CO_2 Laser, L2(1), 31
- Effects of Semiconductor Laser Bias Current on Synchronization in Chaotic Dynamics, 15(4), 11
- Effect of Transverse Magnetic Field on Laser Beam Width Parameter, 8(3), 31
- Fabrication of Solid Random Gain Media in Visible Region from Rhodamine Dye Solutions Containing Highly-Pure Titanium Dioxide Nanoparticles, 18(1), 3
- Femtosecond Ti:sapphire Laser Pulses to Deposit Precious Metal Nanoparticles on Crystalline and Amorphous Titanium Dioxide Films, 14(2), 43
- Gaussian to Super-Gaussian Laser Beam Intensity Profile Conversion using Glass Micro-Optic Fabricated with Reflowed Photoresist, 16(2), 3
- HAZ and Melt Limits of 3-D CO_2 Laser Welding, 7(2), 11
- Improvement of Wound Healing in Rabbit Skin by Low Level Polarized Laser Light, 9(4), 29
- Laser-Assisted CVD Fabrication and Characterization of Carbon and Tungsten Microhelics for Microthrsters, 3(3), 3
- Laser-Controlled Photoluminescence Characteristics of Silicon Nanocrystallites Produced by Laser-Induced Etching, 1(1), 15
- Laser-Human Skin Interaction: Analytical Study and Optimization of Present Non-Ablative Laser Resurfacing, 4(3), 5
- Modeling of 3-D Keyhole CO_2 Laser Welding of Steel, 6(1), 15
- Modeling of Plume Dynamics in Laser Ablation with Application to Nanotubes Synthesis, 16(2), 25
- Modeling of Temperature-Dependent Absorptivity of Laser-Treated Surface, 6(3), 21
- Non-ablative Tattoo Removal Using Fundamental and Second Harmonic Nd:YAG Laser (Histological Observations), 9(4), 11
- Non-Ablative Tattoo Removal Using Fundamental and Second Harmonic Nd:YAG Laser (Tattoo Ink Clearance Response), 10(1), 21
- Optical Properties of Silicon Nanoparticles Produced by Nd:YAG Laser Ablation, 4(4), 19
- Performance Optimization of Multi-Quantum Wells Laser Used in Optical Communications, L2(2), 11
- Profiling of Antimony Diffusivity in Silicon Substrates using Laser-Induced Diffusion Technique, L3(1), 23
- Simultaneous Amplitude-Modulation and Harmonic Frequency-Modulation Mode Locking of Nd:YAG Laser, 16(2), 11
- Structural Characteristics Study of Indium Diffusion in Silicon Using a Pulsed Nd:YAG Laser, 1(1), 34
- Studying of Reflected Light Optical Laser Microscope Images Using Image Processing Algorithm, 9(1), 15
- Temperature Dependencies of Refractive Index and Optical Elasticity Coefficient on Lens Induced in Nd:YAG Crystal, 8(1), 35
- Terahertz Lasing Using Optically Excited Neutral Donor Centres Embedded in Crystalline Silicon, 16(3), 21
- Using Frequency Resolved Optical Gating for Optimization of Thermal Lensing Compensated Ti:Sapphire Femtosecond Laser System, 11(3), 9

Plasma Physics & Applications
IJAP-PPAA

- Advanced Laser Diagnostics for Non-Equilibrium Plasma Assisted Combustion Kinetics, 14(2), 3
- Analysis of Boltzmann Equation for SF6 and Some Gas-Mixture Discharges at Critical Field Condition, 12(1), 31
- Analysis of Secondary Electron Emission in Gas Glow Discharges Used for Thin Film Deposition Processes, 16(1), 15
- Breakdown and Langmuir Electrical Characteristics of Glow Discharge Plasma in DC Reactive Dual-Magnetron Sputtering System, 16(1), 3
- Characterization of Low-Pressure Argon and Nitrogen Discharge Plasmas Using Electrical Floating Probe Method, 9(3), 25
- Current-Voltage Characteristics of DC Plasma Discharges Employed in Sputtering Techniques, 12(3), 10
- Determination of Electron Temperatures in Rare-Gases Plasma, 4(1), 5
- Effect of Adding Nitrogen to the Gas Mixture on Plasma Characteristics of a Closed-Field Unbalanced DC Magnetron Sputtering System, 10(1), 27
- Effect of Annealing on the Electrical Characteristics of CdO-Si Heterostructure Produced by Plasma-Induced Bonding Technique, 4(3), 33
- Effects of Dual-Magnetron Configuration on Electrical Characteristics of Argon Discharge Plasma, 18(3), 17
- Employment of Magnetron to Enhance Langmuir Probe Characteristics of Argon Glow Discharge Plasma in Sputtering System, 12(4), 19
- Generation of Highly-Directed Laser-Driven Plasma Blocks for Light Ion Beam Fusion Applications, 6(1), 3
- Influence of Inter-Electrode Distance, Gas Mixing, Magnetic Field and Cathode Material on Breakdown Voltage of Lab-Made DC Magnetron Sputtering Device, 10(4), 21
- Influence of Magnetic Nitrogen Plasma Functionalization of High Density Polycarbonate, 8(4), 17
- Isentropic and Isenthalpic Cooling Techniques for Low-Temperature Discharges, 15(4), 29
- Langmuir Probe Diagnostics of Low-Pressure Glow Discharge Plasma Using Argon-Nitrogen Mixtures, 12(2), 17
- Laser-Based Measurements in Non-Equilibrium Plasmas, 8(1), 3
- Magnetic Field Distribution of Closed-Field Unbalanced Dual Magnetrons Employed in Plasma Sputtering Systems, 12(3), 35
- Microhardness and Tension Measurements of Pulsed-Laser Surface-Treated Aluminum Alloys, 11(3), 21
- Monte Carlo Simulation of Electronic Kinetics in Gas Discharge, 1(3), 3
- Numerical Model to Estimate the Potential Changes within Laser-Solid Surface Interaction Zone, 6(2), 3
- One-Dimension Simulation of Plasma Flow in the Cylindrical Hall Thruster, 8(4), 23
- The Fundamentals of Plasma-Assisted CVD Technique Employed in Thin Films Production, L1(2), 3

All Rights Reserved ISSN (printed) 1813-2065, (online) 2309-1673 Printed in IRAQ

Quantum Physics & Spectroscopy

IJAP-QPAS

- Alternative mechanisms for electroweak symmetry breaking, 8(2), 8
- Application of Hydrotropic Solubilization Phenomenon for Estimating Diacerein in Capsule Dosage Form by Spectrophotometry Methods, 8(3), 17
- Beating Classical and Quantum Limits in Optics, 3(2), 3
- Calculation of Charge Density Distribution of (2s-1d) Shell-Model Nuclei Using the Occupation Numbers of States, 2(1,2), 31
- CERN experiments observe particle consistent with long-sought Higgs boson, 8(3), 11
- Characterization of Highly-Pure Silicon Dioxide Nanoparticles as Scattering Centers for Random Gain Media, 16(2), 37
- Correction Four-Component Dirac-Coulomb Using Gaussian Basis-Set and Gaussian Model Distribution for Super Heavy Element (Z=115), 12(1), 17
- Design of a Fundamental Concept of Virtual Reality System for Intensity Distribution in Free Electron Laser Amplifier, 4(1), 11
- Dispersion Compensation for a Femtosecond Self-Pumped Phase Conjugator, 2(3,4), 9
- Effect of Acidic Environment on the Spectral Properties of *Hibiscus sabdariffa* Organic Dye used in Dye-Sensitized Solar Cells, 10(2), 27
- Effect of Dissipative Forces on the Theory of a Single-Atom Microlaser, 2(3,4), 12
- Effect of Oxygen Quencher on Absorption and Fluorescence Spectra of Rhodamie-6G and Rhodamine-B Dyes in Ethanol Solvent, 1(1), 20
- Effect of the Scattered Solar Radiation on the Atmospheric Ozone Measurements, 2(1,2), 11
- Effect of Thermal Annealing on Photoluminescence Characteristics of Titanium Dioxide Thin Films Doped with Copper Oxide by Pulsed-Laser Deposition, 17(4), 15
- Effective Collection and Transformation of Emission into Directional Radiation Based on Surface Plasmon-Coupled Emission, 17(1), 21
- Effects of Rare Earth Dopants on Spectroscopic Properties of Silica Glasses Prepared by Sol-Gel Technique, 16(3), 3
- Effects of Solvent Properties on Absorption and Fluorescence Characteristics of Two Organic Dyes Used as Random Gain Media, 17(2), 15
- Effects of Temperature and Concentration on Spectroscopic Behaviors of Laser Dye, 12(1), 35
- Elusive particle may be near, 8(2), 26
- Energy Transfer Calculations Based on Fluorescence Spectra of Acriflavine and Rhodamine B Laser Dyes, 16(3), 33
- Experimental Observations and Modelling of Electron Density of the Plasmasphere, 6(1), 47
- Extra Val Function for the Theoretical Sensing of Ultraviolet Light and Temperature Produced by Fluorescein-Filled Photonic Crystal Fiber, 13(3), 29
- Fluorescence Characteristics of Coated-Cell Dye Solutions Containing Highly-Pure Nanoparticles as Random Gain Media, 18(1), 35
- Fluorescence Characteristics of Highly-Pure Nanoparticles Embedded in Dye Complexes for Random Laser Design, 18(2), 27
- Fluorescence Energy Transfer Characteristics in Binary Acriflavine-Red Nut Lasing Dye Mixtures, 12(2), 3
- Fractal Nanotechnology, 4(4), 25
- FTIR Spectra of Molybdenum Tellurite Glasses, 2(1,2), 23
- FTIR Spectroscopic and Computational Studies on Hydrogen Adsorption on the Zeolite Li–FER, 4(2), 21
- General Characteristics of High Energetic Proton Events Observed with SOHO/ERNE During Solar Cycle 23, 10(4), 3
- Generation of Femtosecond Pulses from Order-of-Magnitude Pulse Compression in a Synchronously Pumped Optical Parametric Oscillator Based on Periodically Poled Lithium Niobate, 2(3,4), 24
- Generation of Intense 8-fs Pulses at 400nm, 2(3,4), 15
- Higgs Boson, 8(2), 3
- High-Intensity Third-Harmonic Generation in Beta Barium Borate Through Second-Order and Third-Order Susceptibilities, 2(3,4), 18
- Introduction to the Higgs Boson Papers, 8(2), 12
- Introduction to Particle Physics and the LHC, 8(2), 23
- Luminescence Characterization of the Bio-Conjugated Quantum Dots with CA125 Antigen Using Linkage Molecules, 7(1), 27
- Luminescent Plates Doped with Stilbene 420 Dye for Enhanced Silicon Solar Cell Performance: Down-Conversion, 6(4), 3
- Measurements of *d*-band Center Shifts of Titanium Dioxide Catalyst Using Gold Nanoparticles in Carbon Monoxide Oxidation Reaction, 14(3), 3
- Measurement of Water Vapour and Temperature Profiles Within the Troposphere Using Ultraviolet Raman LIDAR System, 8(1), 19
- Medium Energy Ion Scattering Spectrometry of Helium Ions Scattered from Rutile Titanium Dioxide Surfaces, 14(3), 29
- Nanolasers: Lasing from Nanoscale Quantum Wires, 3(4), 3
- Near-Edge X-ray Absorption Fine Structure Analysis of Magnesium-Palladium Nanoparticles Fabricated by Gas Evaporation Method, 14(3), 35
- Optical Emission Spectroscopy of Laser-Produced Plasmas of Some Metal Targets, 18(1), 15
- Optimization and Fine-Tuning of Controlled White-Light Continuum Generation in Transparent Solid Medium by 1-kHz Repetition Rate Femtosecond Laser Pulses, 12(1), 27
- Phase Conjugation with Random Fields and with Deterministic and Random Scatterers, 2(3,4), 21
- Preparation and Characterization of Dysprosium-Doped Titanium Dioxide Photocatalyst by Sol-Gel Method, 17(3), 3
- Silicon Dioxide Nanostructures-Coated External Cavity for Gain Enhancement of Rhodamine B Lasing Dye, 14(1), 3
- Some Physical Properties of Metal-Hydroxyquinoline Complexes in Different Solvents, 17(1), 9
- Spectroscopic Study of Chromium-Doped Silicon Nitride Nanostructures Prepared by DC Reactive Magnetron Sputtering, 17(2), 11
- Spectroscopic Study of Sol-gel Synthesized Silica Xerogel Embedded with Dysprosium Ions, 18(4), 3
- Synchronization in Optically Coupled Chaotic Systems by Optical Feedback, 12(1), 11
- Synchrotron-Radiation Infrared Microscopy Analysis of an Amyloid Peptide Irradiated by Mid-Infrared Free-Electron Laser, 14(3), 41
- The biggest machine in the world, 8(2), 22
- The Mythical Higgs Boson, 8(2), 26
- Finding the Smallest Unifying Particle in the Human Universe: An Artistic Theory of Everything, 8(2), 27
- X-Ray Absorption Fine Structure Spectroscopy of Alumina-Supported Copper Oxide for Conversion Electron Yield Detection, 14(4), 29

Semiconductors & Optoelectronics

IJAP-SCAOE

- Analysis and Simulation of Carrier Transport in InP-Based Double Heterojunction Photoelectronic Device, 13(3), 23
- Annealing Effect on the Photoluminescence of CdTe/CdSe Thin Film Photovoltaic Devices, 1(3), 23
- Band Diagram of p-PbTe/n-Si Heterostructure, 1(2), 27
- Characteristics of a-Si:H Solar Cell Under Extended Illumination Condition Using NIR Laser, 5(1), 35
- Characteristics of p-n Junction Silicon Carbide LED, 2(1,2), 17
- Characterization of $(CdO)_{1-x}(ZnO)_x$ Thin Films Prepared by Pulsed-Laser Deposition for Solar Cell Applications, 11(3), 3
- Characterization of CdS:In/Si Heterojunction Solar Cells, 1(2), 13
- Characterization of SiC/Si Heterojunction Fabricated by Plasma-Induced Growth of Nanostructured Silicon Carbide Layer on Silicon Surface, 12(2), 9
- Charge Injection into Organic Semiconductors, 4(2), 5

© 2022 Iraqi Society for Alternative and Renewable Energy Sources and Techniques (I.S.A.R.E.S.T.)

Solid State Physics & Applications

IJAP-SSPAA

All Rights Reserved ISSN (printed) 1813-2065, (online) 2309-1673 Printed in IRAQ

* * *

Notes:

- 1(1), 3 refer to IJAP, Vol. 1, No. 1, page 3
- L1(1), 3 refer to IJAPLett, Vol. 1, No. 1, page 3

© 2022 Iraqi Society for Alternative and Renewable Energy Sources and Techniques (I.S.A.R.E.S.T.)

Iraqi Journal of Applied Physics

P. O. Box 55259, Baghdad 12001, IRAQ
www.iraqiphysicsjournal.com
Email: info@iraqiphysicsjournal.com
Email: editor_ijap@yahoo.co.uk
Email: irq_appl_phys@yahoo.com
Email: ijap.editor@gmail.com

Author Index 2005-2022

All Rights Reserved ISSN (printed) 1813-2065, (online) 2309-1673 Printed in IRAQ

© 2022 Iraqi Society for Alternative and Renewable Energy Sources and Techniques (I.S.A.R.E.S.T.)

All Rights Reserved ISSN (printed) 1813-2065, (online) 2309-1673 Printed in IRAQ

© 2022 Iraqi Society for Alternative and Renewable Energy Sources and Techniques (I.S.A.R.E.S.T.)

All Rights Reserved ISSN (printed) 1813-2065, (online) 2309-1673 Printed in IRAQ

© 2022 Iraqi Society for Alternative and Renewable Energy Sources and Techniques (I.S.A.R.E.S.T.)

THE IRAQI JOURNAL OF APPLIED PHYSICS
EDITORIAL BOARD

COPYRIGHT RELEASE FORM
IRAQI JOURNAL OF APPLIED PHYSICS (IJAP)

We, the undersigned, the author/authors of the article titled

……
……
……
……
……
……
……

that is submitted to the Iraqi Journal of Applied Physics (IJAP) for publication, declare that we have neither taken part or full text from any published work by others, nor presented or published it elsewhere in any other journal. We also declare transferring copyrights and conduct of this article to the Iraqi Journal of Applied Physics (IJAP) after accepting it for publication.

The authors will keep the following rights:

1. Possession of the article such as patent rights.
2. Free of charge use of the article or part of it in any future work by the authors such as books and lecture notes after informing IJAP editorial board.
3. Republishing the article for any personal purposes of the authors after taking journal permission.

To be signed by all authors:

Signature:……..date: ……
Printed name: ……

Signature:……..date: ……
Printed name: ……

Signature:……..date: ……
Printed name: ……

Correspondence author:……..……..……...
……
Address:……..……
……
Telephone:……..……..email: ……

Note: Complete and sign this form and mail it to the below address with your finally revised manuscript

The Iraqi Journal of Applied Physics
www.iraqiphysicsjournal.com
Email: info@iraqiphysicsjournal.com
Email: editor_ijap@yahoo.co.uk
Email: ijap.editor@gmail.com

IRAQI JOURNAL OF APPLIED PHYSICS
Volume (18) Issue (4) October-December 2022

CONTENTS